Overcoming Critical Design Challenges of Wind Turbines

Opklaring af kritiske designmæssige udfordringer for vindmøller

EUDP journal nr.: 64011-0346

Final Report

Edited by Frederik Zahle
3 November 2014

Contents

1 Project Details

Project Title	Overcoming Critical Design Challenges of Wind Turbines
Project identification (program abbrev. and file)	WTopt, journalnr.: 64011-0346
Name of the programme which has funded the project	EUDP
Project managing company/institution (name and address)	DTU Wind Energy, Frederiksborgvej 399, 4000 Roskilde
Project partners	Siemens Wind Power, LM Wind Power
CVR (central business register)	30060946
Date for submission	31.10.2014

2 Short Description of project objective and results

English Summary: The objective of the project was to develop, demonstrate and implement new models, tools and experimental techniques to reduce the uncertainty associated with design of wind turbines ultimately reducing their cost. Four areas of research were addressed: Design and validation of new thick aerofoils, where measurement uncertainty was reduced through detailed characterization of the LM wind tunnel, demonstrated on a new thick aerofoil; extraction of 3D aerofoil data for thick high lift aerofoils and implementation of a new CFD model for vortex generators; Identification of key mechanisms governing blade vibration at standstill though state-of-the art fluid-structure interaction simulations; Identification of the importance of elastic couplings for enhanced load alleviation characteristics of blades where new models were implemented to model these effects correctly.

Dansk Sammendrag: Målsætningen med dette projekt var at udvikle, demonstrere og implementere nye modeller, værktøjer samt eksperimentelle teknikker med det formål at reducere usikkerhederne forbundet med design af vindmøller og dermed muliggøre en reduktion af deres pris. Fire forskningsområder blev udvalgt: design og validering af tykke vingeprofiler, hvor usikkerheden blev reduceret igennem detaljeret karakterisering af LMs vindtunnel, valideret på et nyt vingeprofil; beregning af 3D profildata for tykke vingeprofiler og implementering af en ny CFD model for vortex generatorer; Identifikation af de nøglemekanismer, der styrer stilstandssvingninger af vinger igennem et nyudviklet fluid-struktur beregningsværktøj; Identifikation af indflydelsen af elastiske koblinger for at forbedre vindmøllevingers lastreduktionsegenskaber, hvor nye modeller er blevet implementeret for at beskrive disse egenskaber med højere nøjagtighed.

3 Executive Summary

The aim of the project Overcoming Critical Design Challenges of Wind Turbines was to address a number of key challenges currently faced in research and development of wind turbines. Utilizing state-of-the-art industry-driven experimental facilities and applying high-fidelity research methods new tools and models were developed and implemented that will enable the industry partners to meet these challenges.

Design and validation of new thick aerofoils

Thick aerofoils ranging up to 40% relative thickness are being increasingly used on modern megawatt turbines to reduce mass and increase stiffness, and to facilitate this trend, Work Package 1 aimed at addressing some of the uncertainties related to design of and measurements on thick aerofoils. More specifically, detailed flow quality measurements were conducted in the LM Wind Power wind tunnel mapping turbulence intensity and wall boundary layers, and techniques for suppressing wall-effects were explored. This was supported by 3D CFD simulations of the wind tunnel. Finally, a new 40% thick aerofoil was designed using CFD and tested in the LM wind tunnel.

Identification of 2D/3D thick aerofoil data for rotating wind turbine blades

While aerofoils are typically designed and tested assuming quasi two-dimensional flow conditions, this is far from the conditions they operate under on rotating wind turbine blades. Therefore, corrections are applied taking into account three-dimensional effects due to rotation which are dominant in the root region of a wind turbine blade. Work Package 2 explored different high lift solutions such as Gurney flaps and vortex generators for the inner part of the rotor and utilized 3D CFD to extract aerofoil characteristics along the blade, which were compared to conventional models for 3D corrections as well as data from the DANAERO experiment.

Identification of the standstill problem

Turbine failures at standstill have in recent years been reported by industry. Yet, considerable uncertainty is still associated with calculation of standstill loads. In Work Package 3 increasing the knowledge about the root of standstill vibrations was approached from several directions: 3D CFD as well as wind tunnel measurements were used to derive 360 degree aerofoil data used in aeroelastic simulation codes. Secondly, a newly developed framework coupling high fidelity 3D CFD with the structural model of an aeroelastic code was used to explore the complex aeroelastically coupled dynamics of a blade at standstill. This work successfully identified that vortex induced vibrations can occur on wind turbine blades, which is a phenomenon that cannot be modelled using normal aeroelastic codes.

Identification of the importance of elastic couplings

The accurate estimation of the structural properties of wind turbine blades is paramount for a correct evaluation of the aeroelastic performance of wind turbine blades. However, elastic coupling effects stemming from the anisotropic properties of the laminates and geometrical shape of the blade are partially neglected in present state-of-the-art aeroelastic codes. New development of the structural models in BECAS and HAWC2 has now enabled the study of these effects in a design context. A design study was conducted in which the layup angles of the material in the blade were tailored to obtain up to 10% reduction in the blade flapwise fatigue loads, while minimising changes in stiffness compared to the original blade.

4 Project Results and Dissemination of Results

This chapter describes the work carried out in the four work packages. The individual sections are often condensed versions of work published at conferences and in journal papers, which the interested reader can refer to for greater detail.

4.1 List of Publications

- J. Heinz, N. Sørensen, and F. Zahle. Fluid-Structure Interaction Computations for Geometrically Resolved Rotor Simulations Using CFD (in review process). Wind Energy, 2014.
- J. Heinz, N. Sørensen, F. Zahle, and W. Skrzypinski. Vortex-Induced Vibrations on a Modern Wind Turbine Blade (in review process). Wind Energy, 2014.
- W. Skrzypinski, F. Zahle, and C. Bak. Parametric approximation of airfoil aerodynamic coefficients at high angles of attack. In European Wind Energy Conference & Exhibition 2014, 2014.
- W. Skrzypinski, M. Gaunaa, N. Sørensen, F. Zahle, and J. Heinz. Vortex-induced vibrations of a du96-w-180 airfoil at 90 deg angle of attack. Wind Energy, 17(10):1495–1514, 2014. ISSN 1099-1824. doi: 10.1002/we.1647. URL http://dx.doi.org/10.1002/we.1647.
- W. R. Skrzypinski, M. Gaunaa, N. Sørensen, F. Zahle, and J. Heinz. Self-induced vibrations of a du96- w-180 airfoil in stall. Wind Energy, 17(4):641–655, 2014. ISSN 1099-1824. doi: 10.1002/we.1596. URL http://dx.doi.org/10.1002/we.1596.
- N. Troldborg, C. Bak, N. Sørensen, H. Madsen, P.-E. Rethore, F. Zahle, and S. Guntur. Experimental and numerical investigation of 3d aerofoil characteristics on a MW wind turbine. EWEA, Vienna, Austria, 2013.
- N. Troldborg, N. Sørensen, F. Zahle, and P.-E. Rethore. Simulation of a MW rotor equipped with vortex generators using CFD and an actuator shape model. 53rd AIAA Aerospace Sciences Meeting, AIAA Science and Technology Forum 2015, 2015.
- N. Troldborg, N. Sørensen, P.-E. Rethore, and M. Laan. A consistent method for finite volume discretization of body forces on collocated grids applied to flow through an actuator disk. To be submitted for Journal of Computers and Fluids, 2015.
- F. Zahle, C. Bak, S. Guntur, N. Sørensen, and N. Troldborg. Comprehensive aerodynamic analysis of a 10 MW wind turbine rotor using 3D CFD. 32nd ASME Wind Energy Symposium, 2014.

4.2 WP1: Design and Validation of New Thick Aerofoils

Author(s): Andreas Fischer, Joachim Heinz, Frederik Zahle, Niels N. Sørensen

The increasing size of wind turbine rotors requires higher stiffness of the airfoil sections. This can be achieved by increasing the airfoil thickness. Only a few public thick airfoils exist and the precision of the flow models used for their design are uncertain for airfoils with this thickness. Additionally, experimental derivation of airfoil data for thick airfoils is also associated with high uncertainty. Therefore, both design tools and experimental techniques to establish airfoil characteristics need to be improved. This work package will address both aspects: Based on wind tunnel tests including advanced flow visualization and corresponding 3D CFD simulations, recommendations of how to carry out tests on thick airfoils will be derived; Using state-of-the-art design tools an efficient thick airfoil will be designed and tested in a wind tunnel according to the recommendations formulated.

The following sections describe the work carried out towards reaching these goals.

4.2.1 Boundary Layer and Turbulence Measurements in the LM Low Speed Wind Tunnel

Motivation

Testing thick aerofoils in a wind tunnel is more challenging than testing thin aerofoils, because they create a greater disturbance of the flow field in the test section. These disturbances can have influence on the flow turbulence and the boundary layers in the test section. Hence, measurements are necessary to characterise the flow field. The measurements of the boundary layer thickness and the inflow turbulence can be directly used to describe the boundary conditions for CFD computations and improve the accuracy.

Wind Tunnel Layout

The LSWT is a closed circuit wind tunnel with a closed test section, figure 4.1. The flow is driven by a

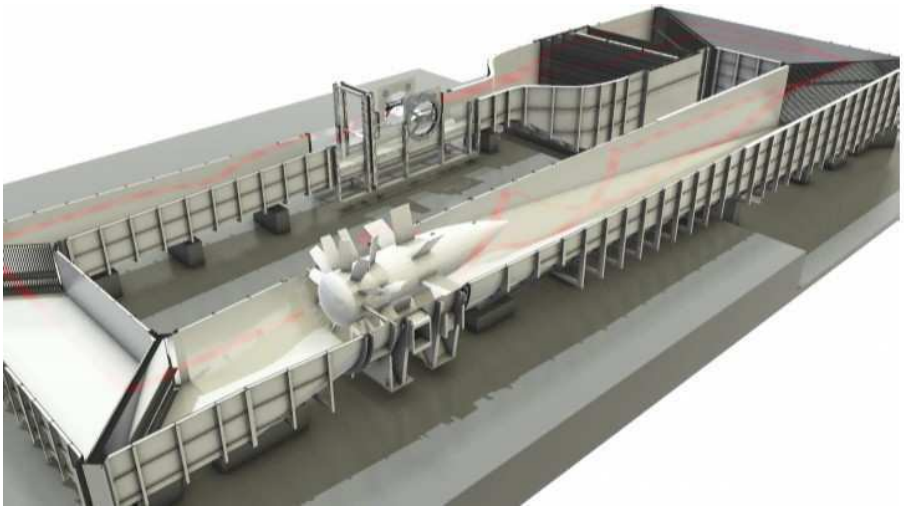

Figure 4.1: The wind tunnel of LM Wind Power A/S (LSWT) (from [5])

1 MW fan. A flow speed of up 105 m/s can be reached. The tunnel is equipped with a heat exchanger which can cool down the fluid to keep the temperature at a constant level. The flow is conditioned with aerodynamically treated corner vanes, a honeycomb structure, 3 screens and a nozzle with a contraction ratio of 10 to 1. The test section is 7 m long and has a cross section of 1.35 m of width and 2.7 m of height. The aerofoils tested in the wind tunnel span the width and are mounted between two turn tables. The centre of the turn table is 3.0 m downstream of the beginning of the test section.
The measurements were carried out in the empty wind tunnel and with inserted flatback aerofoil. The

aerofoil model was a FFA-W3-400FB with a chord length of 0.6 m. The maximum thickness was 40% and the trailing edge thickness was 33.5 mm. The centre of rotation was at 35% of the chord length.

Boundary Layer Measurements

The boundary layer mean flow was measured with a so called boundary layer rake consisting of Pitot and total head tubes. The boundary layer rake was attached to the wall with double sided tape, figure 4.2. It

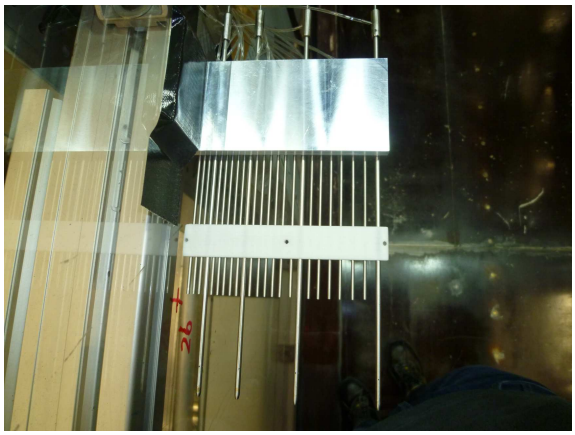

Figure 4.2: The boundary layer rake.

consists of 20 total head tubes and 4 Pitot tubes (total head and static pressure). The total head tubes have a length of 130 mm and a diameter of 2 mm. The Pitot tubes have a length of 250 mm and a diameter of 3 mm. The static pressure holes are 15 mm downstream of the tip. The measurement position closest to the wall was 6 mm away and the most outboard measurement position was 114.9 mm away from the wall.
Figure 4.3 shows the development of the boundary layer along the walls of the empty wind tunnel in streamwise direction. The boundary layer grows as expected in streamwise direction. It is thinner at

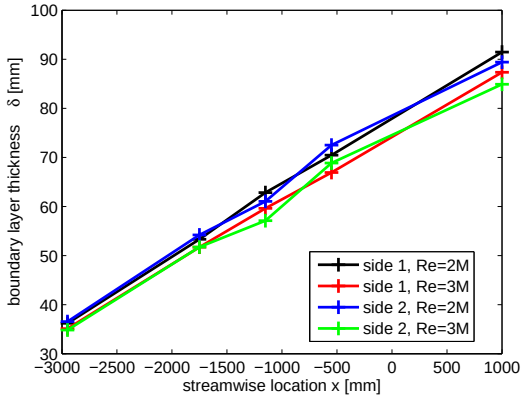

Figure 4.3: Development of the boundary layer thickness in streamwise direction in the empty wind tunnel. x = 0 mm at the centre of the turn table.

Reynolds number 3 million than at Reynolds number 2 million. There is no significant difference between the boundary layer at the two sides of the wind tunnel.
The influence of the aerofoil model on the boundary layer thickness at a position 1150 mm upstream of the centre of the turn table is shown in figure 4.4. At the outer side the boundary layer thickness is not changed by the presence of the aerofoil and the variation with changing angle of attack are within the measurement uncertainty. On the inner side the boundary layer thickness changes when the aerofoil goes from negative to

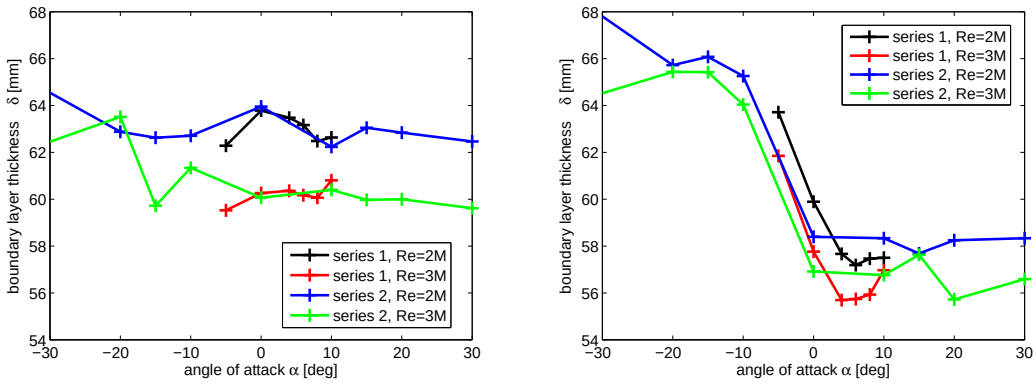

(a) Outer side

(b) Inner side

Figure 4.4: Boundary layer thickness 1150 mm upstream of the turn table centre as function of the angle of attack of the aerofoil.

positive angles of attack. Two different measurement series after removing and remounting the boundary layer rake were undertaken to document the repeatability of the measurement.

Inflow Turbulence

The inflow turbulence was measured with a hot wire system consisting of a Dantec Streamline CTA bridge and signal conditioner, a 16 bit A/D board of National Instruments type e series, a miniature single wire probe (Dantec 55P11) and a Dantec temperature probe. Only the streamwise component of the velocity can be measured with this setup. The hot wire probe was placed on a traversing system, figure 4.5. The

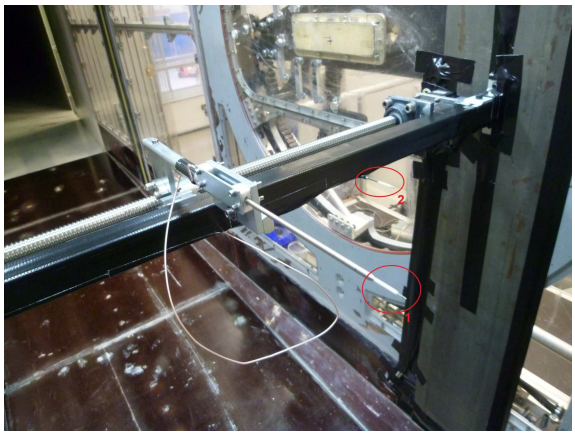

Figure 4.5: The hot wire probe and traversing system. 1 : hot wire probe, 2 : temperature probe.

traversing system is mounted on a rectangular beam with the cross sectional dimension 40 mm x 40 mm spanning the width of the tunnel. It is driven by a stepper motor type ST5709 from NANOTEC with an angular resolution of 400 steps per revolution. The movement is transmitted by an Eichenberger carry ball screw. The thread has a diameter of 25 mm and an inclination of 5 mm.
The spectra of the velocity measured in the empty wind tunnel are displayed in figure 4.6 at a position of 900 mm upstream of the turn table centre.

We show the spectra of the 10 Hz high pass filtered time series as well, because it is common practise to exclude very low frequency fluctuations from turbulence measurements. The spectra show some distinct peaks. Those peaks might originate from structural vibrations. It is not a characteristic of turbulent flow. Hence, the real turbulence intensity in the wind tunnel is lower than the measured one. Most of the

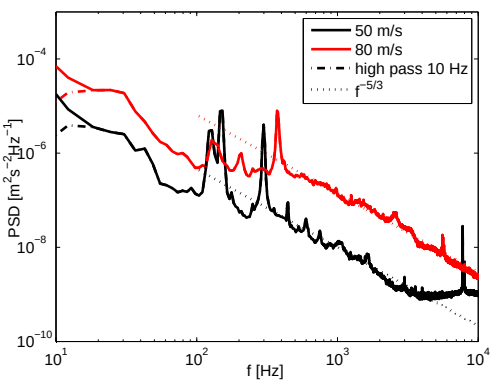

(a) PSD (one-sided)

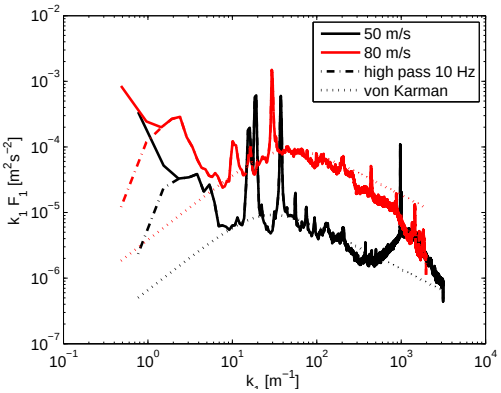

(b) Premultiplied one point spectrum (two-sided)

Figure 4.6: Spectra of the inflow turbulence in the empty wind tunnel at a position 900 mm upstream of the turn table centre.

spectral energy is contained in the low frequency range. The PSD, figure 4.6a, decays as $f^{-5/3}$ in the high frequency range. This is in agreement with Kolmogorov's theory.
In figure 4.6b the theoretical von Karman spectrum is plotted together with the measured data. The length scale L and the variance of the streamwise velocity component $\langle u_1^2 \rangle$ are adjusted in order to fit the von Karman spectrum to the measurements. The length scale was chosen to fit to the global peak value of the measured spectrum. The variance of the streamwise velocity component was chosen in a way that the level of the von Karman spectrum matched the level of the measured spectrum for frequencies higher than the global peak frequency. This variance was lower than the variance of the measured and 10 Hz high pass filtered time series, because the level of the von Karman spectrum for very low frequencies is by decades lower than the measured one.
The premultiplied one point spectra for the empty wind tunnel and in the cases with inserted aerofoil at different angles of attack is presented in figure 4.7. The presence of the aerofoil changes the spectra in

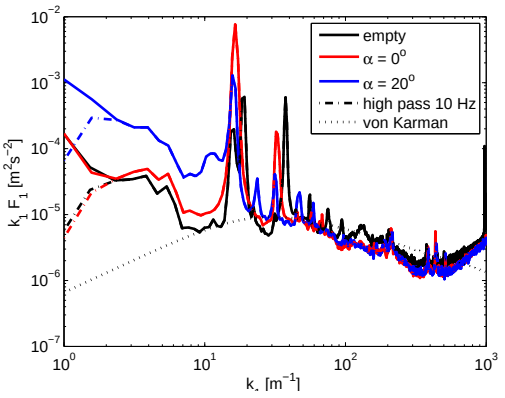

(a) 50 m/s

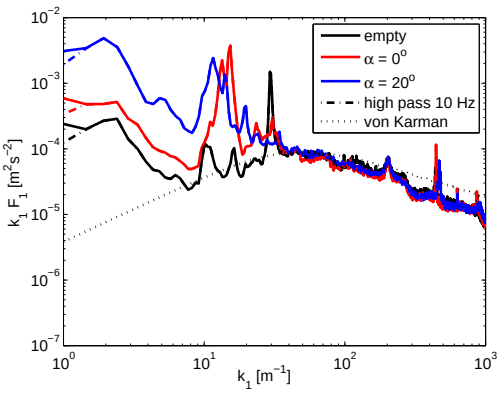

(b) 80 m/s

Figure 4.7: Premultiplied one point spectra of the inflow turbulence at a position 900 mm upstream of the turn table centre.

the low wave number range. For both flow speeds the changes are effective at $k_1 < 40$ 1/m. When the aerofoil is at $\alpha = 0°$ there is a small increase of the spectral energy for the low wave numbers. When it is at $\alpha = 20°$, the increase is considerable. However, it might be a combined effect of enhanced turbulence and enhanced structural vibrations.
The values of the resulting turbulence intensity measured at a position 900 mm upstream of the turn table centre are summarised in table 4.1. The values of the turbulence intensity in the empty wind tunnel we found are by a factor 2 lower than the ones reported during the commissioning of the wind tunnel [32].

run no. [-]	flow speed [m/s]	angle of attack [deg.] (empty tunnel: none)	Ti orig. [%]	Ti hp 10 Hz [%]
3	50	none	0.100	0.045
4	80	none	0.099	0.050
6	50	0	0.117	0.075
7	50	20	0.250	0.079
8	80	0	0.125	0.068
9	80	20	0.211	0.126

Table 4.1: Turbulence intensity at a position 900 mm upstream of the turn table centre.

The new values are supposed to be more accurate, because we used a single wire instead of an x-wire (the x-wire consists of two wires with can shed turbulence on each other), the hot wire equipment we used is more modern and state of the art and the traversing system was specially designed to minimise structural vibrations. The accuracy of CFD computation profits from these new measurements.

4.2.2 Wind Tunnel CFD Modelling

Wind tunnel tests for thick aerofoils are particular challenging. Already at very low angles of attack the aerofoil flow encounters a relatively high negative pressure gradient which makes the flow likely to separate. Additionally, close to the side walls of the wind tunnel test section, the flow properties such as flow velocity and turbulence level are heavily influenced by the presence of the wall. The reduced flow velocity close to the wall makes it particularly difficult for the flow to overcome the high pressure gradients of the thick aerofoil. As a result big separation bubbles can build up at the vicinity of the wind tunnel walls and heavily influence the stall behaviour of the tested aerofoil section. A respective flow situation could look like illustrated in Figure 4.8 showing an exemplary CFD simulation result for the FFA-W3-400FB aerofoil with a chord of $c = 0.6\,m$, an incoming wind speed velocity of $V = 50\,m/s$ and an angle of attack of $AOA = 5\,^{\circ}$.

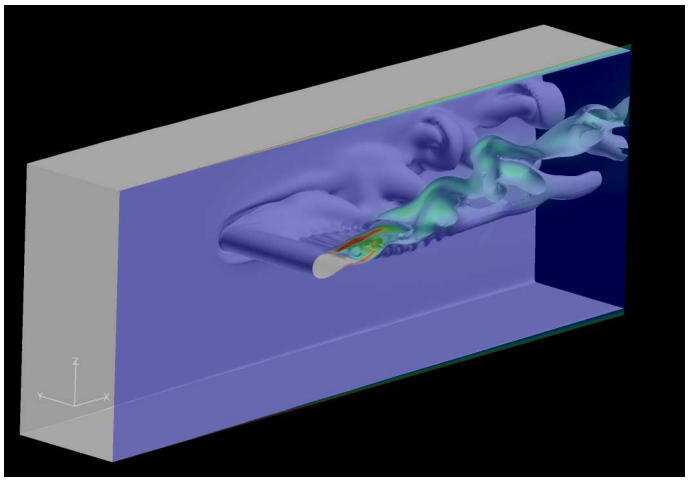

Figure 4.8: Severe Flow Separation of a Thick Airfoil in a Wind Tunnel Simulation with EllipSys3D

It was intended to conduct high-fidelity CFD computations in order to support the wind tunnel tests of thick aerofoils in the LM test facility (see Figure 4.1) with valuable input. Accurate CFD simulations can help to identify and analyze the complex flow patterns that develop close to the wall boundaries and can thus help to further improve the current testing procedure for thick aerofoils in the LM wind tunnel. The computations were carried out with the incompressible finite volume CFD solver EllipSys3D [27] [28] [39] which has proven to provide excellent results in various applications [43] [8]
A CFD mesh was generated which resembles the geometries of the utilized test section in the LM wind tunnel. The mesh is shown in Figure 4.9 and employs approximately 14 million mesh cells and cell sizes which are small enough to conduct Direct Eddy Simulation (DES) computations.

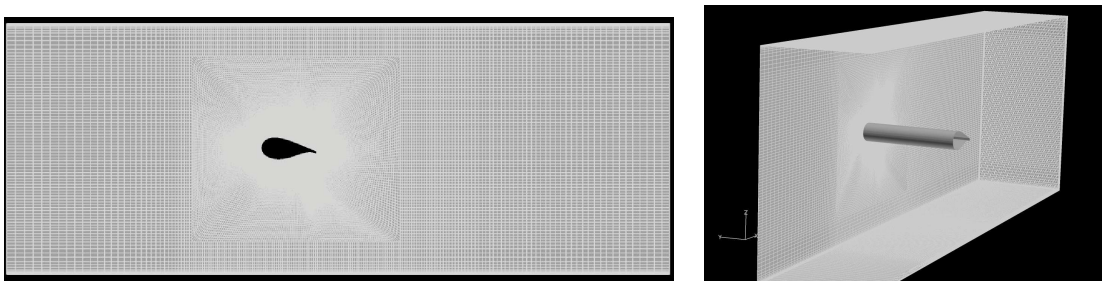

(a) Two-Dimensional View from the Side

(b) Three-Dimensional View

Figure 4.9: CFD mesh of the Wind Tunnel

Accurate CFD simulations of a wind tunnel with highly separated flow are far away from trivial. It was thus decided to use the detailed measurements presented in Section 4.2.1 in order to validate the utilized computational model. Apparently, as indicated in Figure 4.8, the boundary layers at the tunnel walls have

a decisive impact on the overall separation behaviour of the flow past the tested aerofoil section, and a first comparison should therefore identify if the boundary layers of the simulations develop similarly to the ones measured in the tunnel. This was done by using the boundary layer measurements of the most upstream position (Position D: located 2950 mm upstream of turn table center (TTC)) as a prescribed input to the CFD computations and by then comparing the simulation results to the boundary layer measurements which are located further downstream of the wind tunnel (Positions C: 1750 mm upstream of TTC, Position B: 1150 mm upstream of TTC, Position A: 550 mm upstream of TTC, Position E: 1000 mm downstream of TTC, Position F: 2000 mm downstream of TTC). The velocity profile at Position D was prescribed with the analytical formulation of Cole using the friction velocity U_f and the boundary layer thickness δ which both have been determined from the measured data at Position D. Apart from the velocity profile the gradient of the energy dissipation ω and the turbulent kinetic energy k have been prescribed at Position D as well. At areas close to the wall the following expressions have been used

$$\omega = \frac{U_f}{\sqrt{C_\mu} \cdot \kappa \cdot y} \tag{4.1}$$

$$k = \frac{U_f^2}{\sqrt{C_\mu}} \tag{4.2}$$

with y describing the distance to the wall and with the remaining constants set to $C_\mu = 0.09$ and $\kappa = 0.43$. At areas away from the wall the quantities ω and k have been set to values which comply with the relatively low turbulence intensities of the LM wind tunnel.
A first test case was run by simulating the empty wind tunnel without any aerofoil section in the test section. Figure 4.10 shows the comparison between simulation results and measurements for all available measurement positions and it can be seen that the development of the boundary layer along the wind tunnel walls is captured very well by the computations of EllipSys3D.
In a second, more complex test case the wind tunnel is simulated including the flatback aerofoil FFA-W3-400FB of chord $c = 0.6\,m$ and with an angle of attack of $AOA = 4\,^\circ$. The respective comparison to the available boundary layer measurements is shown in Figure 4.11. It can be seen that the conducted simulations fit again very well with the available measurements at Position C and B. No boundary layer measurements were carried out at positions A, E and F while the aerofoil test section was placed inside the wind tunnel: This was because Position A was located too close to the leading edge and the boundary layer in the wake of the aerofoil at Position E and F was considered to be too complex and unstable to provide valuable information for the current state of investigation.

The comparisons of Figure 4.10 and 4.11 demonstrated that the utilized CFD solver EllipSys3D is capable of accurately describing the flow situation of an empty wind tunnel as well as the flow situation in front of a tested aerofoil section. In the next step of the comparison the flow over the actual aerofoil test section is analyzed in more detail. The measurement campaign for the flatback aerofoil FFA-W3-400FB utilized pressure tap measurements located on the center part of the aerofoil where the flow is least influenced from eventual side wall effects. For an angle of attack of $AOA = 0\,^\circ$ the measurements determined a lift coefficient of $C_l = 0.57$ which corresponds to a distributed lift force of approximately $L = 520\,N/m$. Figure 4.12 shows the computed distributed lift force for different assumed wind tunnel widths. For the computation with an infinite tunnel width periodic boundary conditions substitute the no-slip conditions of the walls. The respective simulation results in a constant lift distribution over the entire blade span of approximately $L = 520\,N/m$ and thus confirms the result from the wind tunnel measurements. Introducing wall boundaries to the simulation clearly affects the computed force distribution. For the two simulation setups with tunnel wall distances of 1.80 m and 1.50 m, respectively the lift force still reaches the measured value of approximately $L = 520\,N/m$ in the center of the aerofoil. However, a further reduction of the width to the actual tunnel width of 1.35 m shows a very severe impact on the computed lift force. Hence, by narrowing down the wind tunnel widths by only 0.15 m the computed lift force at the center of the aerofoil drops severely and is suddenly 30% lower than the measured quantity. The simulation thus heavily over-predicts the influences of the wall boundaries and shows regions of heavy flow separation leading to a severe under-prediction of the produced lift on the tested aerofoil section.

Several attemps have been undertaken in order to improve the presented result. Changing the level of inflow turbulence and changing the sensitivity of the employed correlation based transition model of Menter [25]

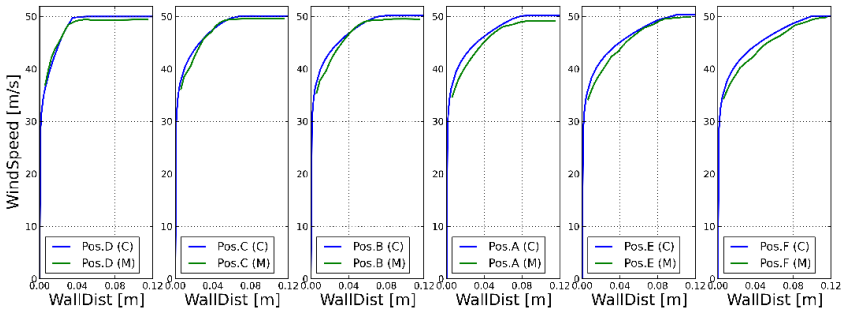

(a) Measurements and Simulations at the Left Tunnel Wall

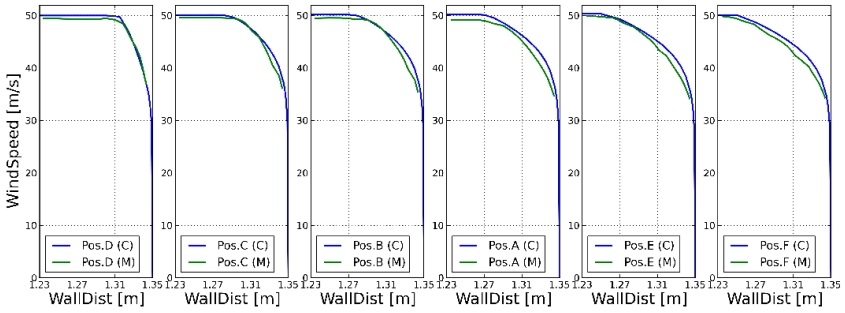

(b) Measurements and Simulations at the Right Tunnel Wall

Figure 4.10: Comparison of the Velocity Profiles for the Empty Wind Tunnel

[26] shows the most decisive impacts on the results. However, those changes did not lead to a consistent improvement which are then also valid for simulations of aerofoils with other angles of attack. It was thus concluded that the employed transition model of Menter is not capable of reliably predicting transition for the complex test case of a thick aerofoil in a relatively narrow wind tunnel. Further investigations on isolated two-dimensional aerofoil sections revealed weaknesses of the Menter model when it comes to the prediction of flows with high Reynolds numbers. This could be the reason why the model fails in the wind tunnel setup where high Reynolds numbers occur along the tunnel walls.
The difficulties encountered in the wind tunnel simulations lead to the implementation of a more complex but better suited e^n type of transition model [45]. A e^n type of model is difficult to implement in general purpose CFD solvers and is for example not available in commercial CFD packages. However, the actual implementation in EllipSys shows promising results for the two-dimensional aerofoil simulations in high Reynolds numbers flows and is currently in the process of being implemented and tested in a three-dimensional context as well. In the future this should facilitate a better prediction of the complex flow in the above discussed wind tunnel setup for thick aerofoils.

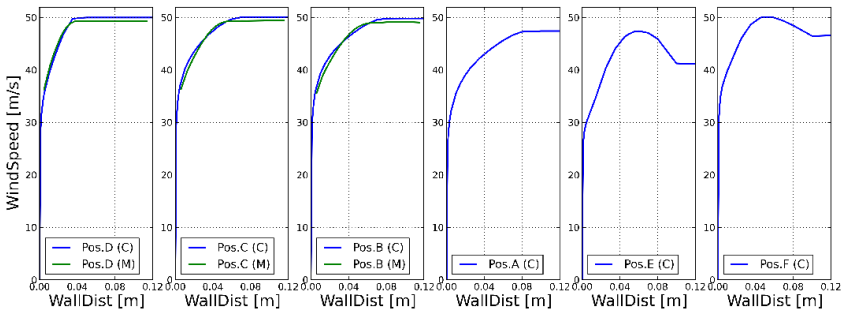

(a) Measurements and Simulations at the Left Tunnel Wall

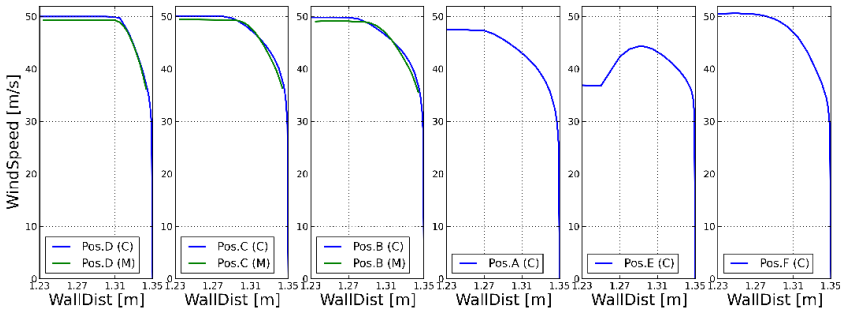

(b) Measurements and Simulations at the Right Tunnel Wall

Figure 4.11: Comparison of the Velocity Profiles for the Wind Tunnel with the FFA-W3-400FB Airfoil at $AOA = 4\,^{\circ}$

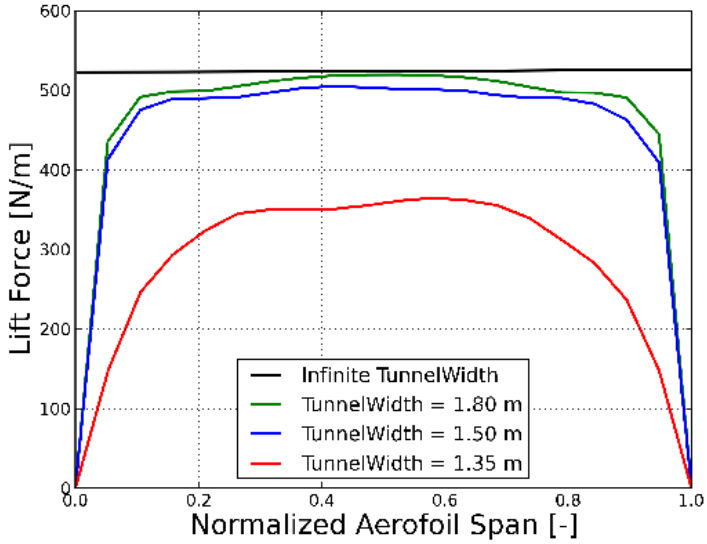

Figure 4.12: Computed Lift Force depending on Wall Distance in Wind Tunnel

4.2.3 Design of a 40% Aerofoil Using 2D CFD

As part of the project a new thick aerofoil was to be designed and subsequently evaluated in the LM Wind Tunnel. The relative thickness of the aerofoil was fixed to be 40%c, since it was to be benchmarked against a modified FFA-W3 aerofoil with relative thickness of 40%c, which was tested in the LM wind tunnel in a previous EUDP project and used extensively by LM to calibrate their wall blowing system. The aerofoil was targeted for operation on a multi-megawatt turbine (diameter D ¿ 100 m) and was thus designed for high Reynolds number operation ($Re = 10 \times 10^6$) even though the LM wind tunnel is only capable of reaching Reynolds numbers of $Re = 4 \times 10^6$. This section describes the design strategy, methods and aerofoils that were designed as part of the project. The design methodology uses a newly developed optimization framework that interfaces to the 2D CFD solver EllipSys2D, which for thick aerofoils is a significant improvement compared to using XFOIL.

Aerofoil Optimization Tool

An aerofoil design tool was developed in this project[1] based on the open source optimization framework OpenMDAO [1]. Two flow solvers were interfaced to the tool: XFOIL, which is a widely used and accurate panel code, and EllipSys2D which is a CFD solver developed at DTU Wind Energy [29, 30, 41]. While XFOIL is very suitable for designing thinner aerofoils of up to 36% relative thickness, it suffers from instability and poor accuracy for thicker aerofoils, which was the focus in this project. An interface to the in-house 2D CFD solver EllipSys2D was thus developed for exploring the possibility of using 2D CFD for optimizing thick aerofoils.

Figure 4.13 shows a flow chart of the different components in the aerofoil optimization using 2D CFD. The optimizer, which based on gradients of the objective and constraints changed the design variables towards an optimal design; the aerofoil geometry builder, which generates a parameterized aerofoil shape; the mesh generator, which takes an aerofoil shape as input and generates a CFD ready mesh; the flow solver which computes the flow over the aerofoil and resulting forces acting on it, and finally the objective function which computes a measure of goodness based on the flow solution.

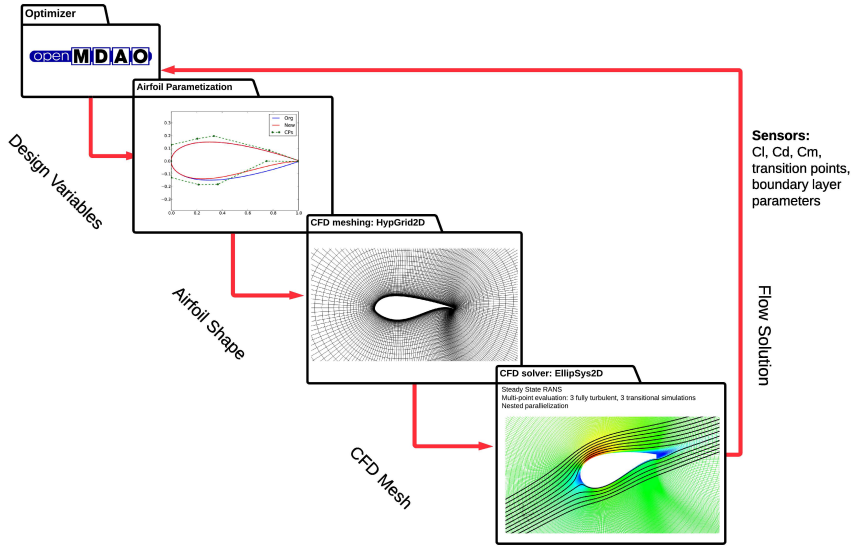

Figure 4.13: Flowchart showing components in optimization framework.

In addition to interfaces to flow solvers, interfaces to a trailing edge noise prediction tool and the cross-sectional structure tool BECAS [9]were developed. While noise is not of concern for thick aerofoils intended for the root sections of a blade, structural characteristics are very important. Figure 4.14 shows a plot of a 30% aerofoil shape and its internal structure computed using BECAS.

[1]Co-financed by the EUDP Light Rotor project no.: 64010-0107

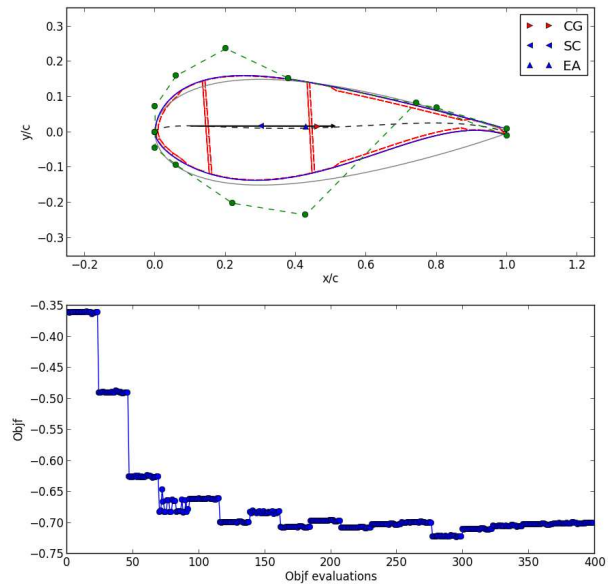

Figure 4.14: Plot showing the iteration history and shape of an aerofoil optimized simultaneously for aerodynamic and structural performance.

Investigation of Shear Web Position

This section describes a study conducted to investigate the influence of the chordwise position of the shear web. The positioning of the shear web impacts both the aerodynamic performance as well as the structural characteristics, which makes it important to map the trade-offs between aerodynamic performance versus structural performance. While on the outer part of the blade, the shear web can be placed more forward in the cross section, it is more desirable to center the shear web for sections closer to the root. The WTopt-40-xc aerofoils were all optimized using the FFA-W3-400FB aerofoil as the initial shape, and since this aerofoil has maximum thickness at x/c=0.25, the ambition with the optimized aerofoils was not to obtain a better aerodynamic performance but instead maximise the performance given the structural constraints chosen.

A shear web of length 30% chord was assumed and constraints were used to ensure a height of 90% thickness at the front and rear web positions. The aerofoils will be referred to as WTopt-40-xc0.XX where XX is [0.30, 0.33, 0.355, 0.38], indicating the midpoint between the two shear webs along the chord.

Table 4.2 summarizes the performance metrics of the four aerofoils. L/D_{max} and C_{l-max} of the aerofoils are almost linearly dependent on shear web chord-wise position with a performance penalty of 22% on L/D of the WTopt-40-xc0.38 compared to the WTopt-40-xc0.30 aerofoil.

Aerofoil name	**Flow type**	$C_l@AOA_{oper}$	$L/D@AOA_{oper}$	C_{l-max}	L/D_{max}
WTopt-40-xc0.30	turb	1.21717(7.00)	45.275	1.509	45.357
WTopt-40-xc0.33	turb	1.15423(7.00)	41.456	1.430	41.669
WTopt-40-xc0.355	turb	1.20454(9.00)	37.625	1.352	38.836
WTopt-40-xc0.38	turb	1.09441(9.00)	34.719	1.280	35.466
WTopt-40-xc0.38GF	turb	1.26878(9.00)	36.862	1.416	38.114
WTopt-40-xc0.38GFnoskew	turb	1.11264(9.00)	30.0	1.26	32.6

Table 4.2: Performance summary for the WTopt-40-xc aerofoils computed at $Re = 9 \times 10^6$.

Table 4.2 also lists the aerofoils WTopt-40-xc0.38GF and WTopt-40-xc0.38GFnoskew which are aerofoils with a Gurney flap added as a design variable. The *noskew* denomination indicates that a constraint was added to reduce the chordwise offset between the suction and pressure side chordwise position of maximum thickness. The addition of a Gurney flap clearly improves the performance of the xc0.38 aerofoil, considerably, whereas the noskew constraint has a tendency to reduce performance.

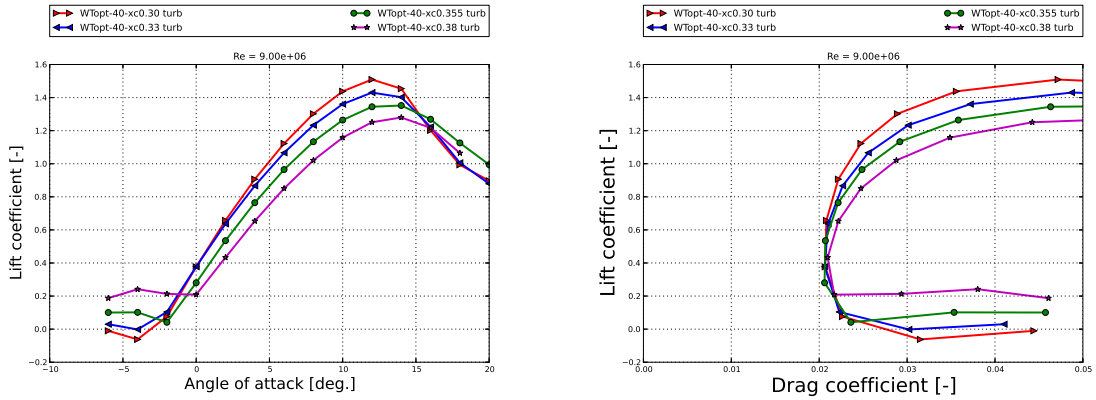

Figure 4.15: Lift and drag polars for the aerofoils design with different shear web positions evaluated at at $Re = 9 \times 10^6$.

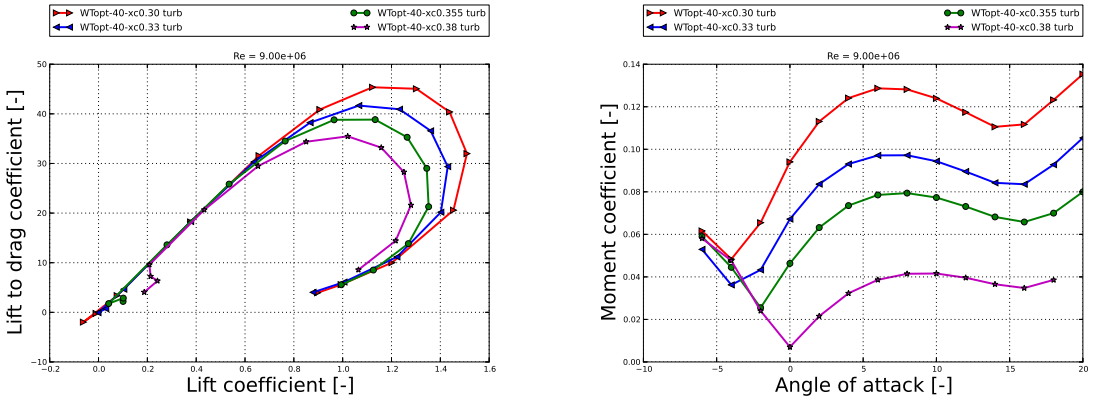

Figure 4.16: Lift to drag and quarter chord moment coefficient for the aerofoils design with different shear web positions evaluated at at $Re = 9 \times 10^6$.

Flatback TE on the xc0.38 Aerofoil

The optimized aerofoils were constrained to a fairly low trailing edge thickness, but investigations on the xc0.38 aerofoil showed that thicker trailing edges in fact resulted in both higher maximum lift coefficients as well as higher lift to drag ratios. The so-called flatback aerofoils are well known and are described several places in literature and are already used in industry. Figures 4.17 show the lift, drag and moment coefficients as well as the lift to drag ratios of the WTopt-40-xc0.38 aerofoil modified with a trailing edge thickness ranging from t/c = [0.08, 0.09, 0.10, 0.11]. While the lift coefficient appears to increase consistently with increasing trailing edge thickness, so does the drag. It can be seen that for the highest thickness of t/c=0.11, the drag increase is significantly greater than for t/c=0.10, which more clearly can be seen in the lift to drag ratio, where the efficiency significantly decreases over most of the C_l range, although the maximum L/D is maintained due to the high C_{l-max}.

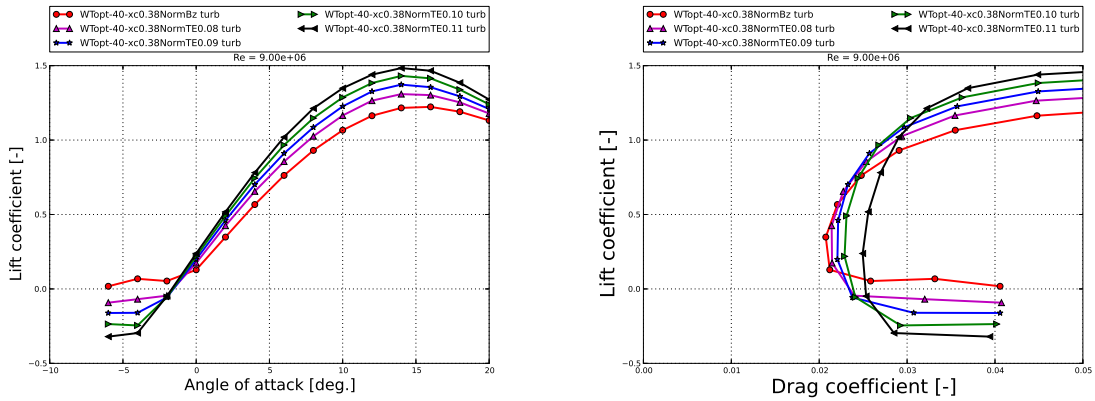

Figure 4.17: Lift and drag polars for the aerofoils design with different shear web positions evaluated at at $Re = 9 \times 10^6$.

Final Aerofoil Choice

The above investigations clearly illustrate the conflicting nature of the structural and aerodynamic objectives in thick aerofoil design. The structurally most compliant aerofoil was chosen, which was the

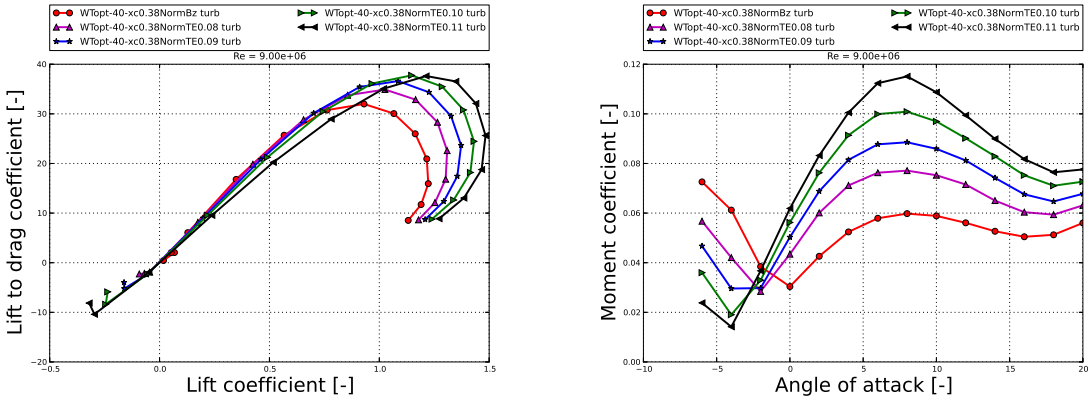

Figure 4.18: Lift to drag and quarter chord moment coefficient for the aerofoils design with different shear web positions evaluated at at $Re = 9 \times 10^6$.

WTopt-40-xc0.38NormTE0.10, due to its very aft position of maximum thickness. Although this aerofoil did not have the best aerodynamic performance it can be improved through the use of vortex generators to increase the maximum lift coefficient.

In Section 4.2.4, a brief overview is provided of the measured performance of the aerofoil in the LM wind tunnel.

4.2.4 Wind Tunnel Testing in the LM Low Speed Wind Tunnel

Author(s): Rolf Hansen (LM Wind Power)

Project objective

The objective of this project for LM Wind Power has been to gain understanding on designing and testing thick airfoils with a relative thickness of above 30%. These airfoils are not only problematic when doing measurements in the LM Low Speed Wind Tunnel (LSWT), but also problematic to predict with CFD tools, which makes it difficult to design and test thick airfoils with high accuracy.

Test Section Improvements

Measurements on thick airfoils above 30% thickness at LSWT are problematic due to 3D effects generated by the side walls in the test section. Therefore a lot of work has been put into smoothening of the side walls in the test section in order to remove surface imperfections that trigger 3D effects. Furthermore the usage of side wall blowing to avoid 3D effects due to side wall boundary flow separation has been assessed. A result from the smoothening and usage of side wall blowers can be seen below, where the FFA-W3-400FB lift polar is shown. The blue curve is the first test done in 2011. The green curve is from 2014.

Wind Tunnel Testing of the Thick Flatback Aerofoil

A new thick aerofoil has also been designed by DTU in corporation with LM Wind Power and tested at the LM LSWT. The aerofoil is 40% thick with a flatback trailing edge. The thickness of the trailing edge is approximately 10% chord. The aerofoil was designed to meet certain geometric constraints, so that it will fit into the LM Wind Power blade portfolio. A result from the test is shown below compared with the FFA-W3-400FB designed in an earlier project.

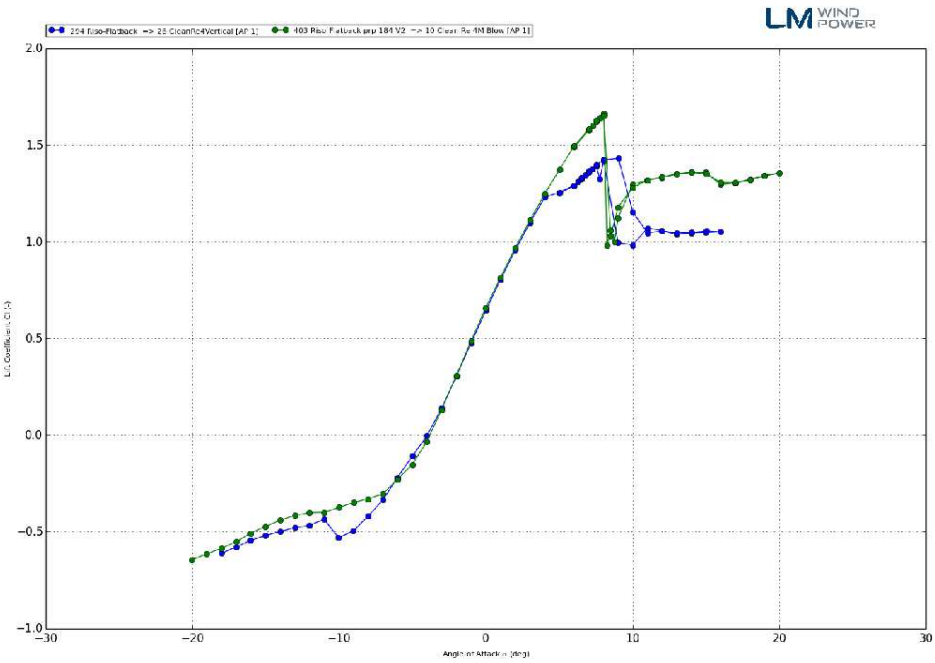

Figure 4.19: Lift curves from two tests on the FFA-W3-400FB airfoil. Blue is from 2011. Green is from 2014 with test section walls smoothened and side wall blowing system active.

It is observed that the lm-14-01-40 aerofoil gives less lift that the FFA-W3-400FB. This was expected as the lm-14-01-40 had to comply with certain geometrical constraints. The drag from the lm-14-01-40 is also higher, which is due to the thicker trailing edge.

Note that the measured data is still being processed and future work will be done to carry out more detailed comparisons between measurements and CFD predictions of the performance of the aerofoil.

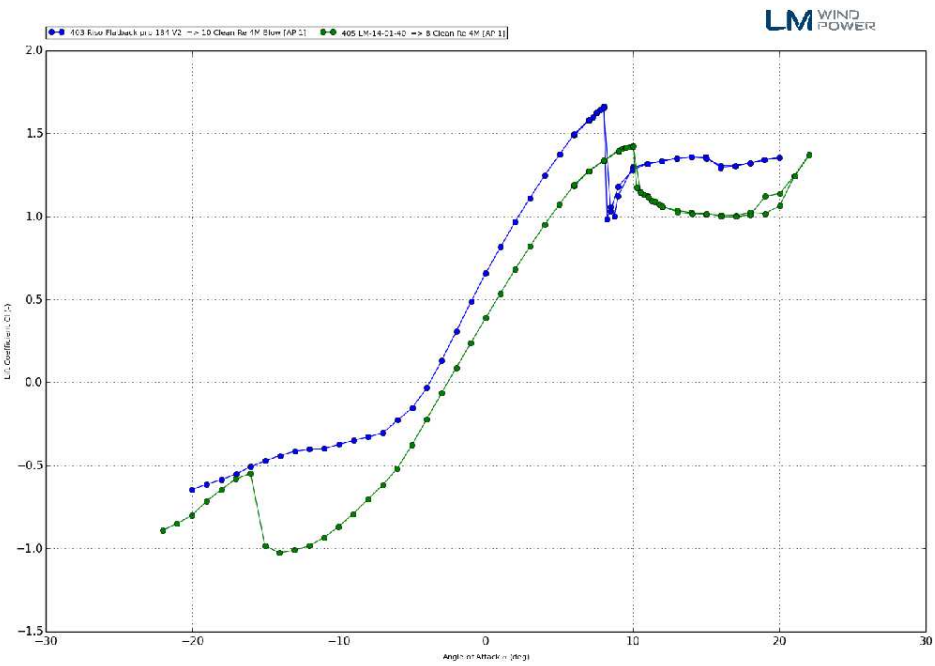

Figure 4.20: Comparison between FFA-W3-400FB and lm-14-01-40 at Reynolds 4 million.

4.3 WP2: Identification of 2D/3D Thick Aerofoil Data for Rotating Wind Turbine Blades

Author(s): Niels Troldborg, Frederik Zahle

Aerodynamic aerofoil characteristics used for design of wind turbines are usually obtained from 2D wind tunnel tests. However, the actual 3D aerofoil characteristics on a rotor can be quite different from those measured in a wind tunnel because of centrifugal forces in the boundary layer, spanwise pressure gradients generated by the Coriolis force as well as unsteady and turbulent inflow conditions. In effect a direct application of the 2D characteristics shows bad agreement between measured and calculated loads especially at the inner part of the blade where the 3D effects are most dominant.
The main objectives of this work package was to investigate 2D/3D aerofoil data for wind turbines with a special emphasis on thick aerofoils with and without stall delaying or lift enhancing devices and based on these investigations to develop a new 3D correction engineering model.

4.3.1 CFD Rotor Simulations in Comparison to DANAERO Full-Scale and Wind Tunnel Measurements

The purpose of this task is to investigate the 3D aerofoil characteristics of a MW wind turbine through a combination of field measurements, wind tunnel tests and computational fluid dynamics (CFD).

Experimental Approach

Two different types of measurements obtained within the DANAERO experiment are used as a basis for the present work:

1) Pressure and inflow measurements on one of the LM38.8 blades on the NM80 2 MW turbine. Surface pressure distributions were measured at the four radial stations, r/R=0.325, 0.475, 0.750 and 0.925 where the relative thickness of the aerofoils was 33%, 24%, 20% and 19%, respectively. Each of the four sections were instrumented with 64 pressure taps. Inflow measurements were provided from a met mast located nearby and from four five-hole Pitot tubes mounted at r/R=0.36, 0.51, 0.78 and 0.90, respectively.
2) 2D wind tunnel measurements on four aerofoils with nearly the same geometry as the four blade sections on the LM38.8 blade which were instrumented with pressure taps.
These data creates a basis for studying how the aerodynamic characteristics on a real wind turbine deviates from those obtained in 2D in a wind tunnel.

Computational Approach

Two different types of simulations are carried out using the in-house incompressible finite volume Reynolds Averaged Navier-Stokes (RANS) flow solver EllipSys [27, 28, 39]:

1) 2D steady state simulations on the four aerofoil sections using the $k-\omega$ SST turbulence model [24] and a correlation based transition model [25, 26, 42].The grids used for the simulations were of the O-mesh type. The domain height was set to approximately 30 chord lengths and the height of the first cell adjacent to surface was set to 10^{-6} chord lengths corresponding to a maximum y^+ of approximately 0.2. All grids had 256 cells around the aerofoil and 128 cells normal to the aerofoil.

2) 3D rotor computations on the NM80 turbine in steady and uniform inflow using the same turbulence and transition models as used for the 2D simulations. In the simulations the rotor geometry and the blade surface boundary layer is fully resolved using a standard O-O mesh configuration. The radius of the domain was approximately 10 rotor diameters and the height of the first cell adjacent to the blade surface was set to satisfy the condition $y^+ < 1$ as required for this type of computations. The blades of the turbines were resolved with $256 \times 128 \times 128$ cells in the chordwise, spanwise and normal direction, respectively. The grid consisted of about $14 \cdot 10^6$ grid cells. These computed data can be considered analogous to the experimental datasets and forms a basis for studying the difference between 2D and 3D aerofoil characteristics.

Comparison of 2D and 3D Aerofoil Characteristics

In order to compare 2D and 3D aerofoil characteristics it is necessary to determine the angle of attack (AoA) at the different blade sections on the rotor blade. Several methods have been proposed for this purpose. Here we use the azimuthal averaging technique (AAT) employed by Hansen and Johansen [31, 19] in which the velocity, at a given radial position in the rotor plane, is calculated using the azimuthally averaged velocity at axial positions up and downstream of the rotor. Since the AAT requires information about the velocity field both up and downstream we can not use it to estimate the AoA from the measurements. Instead the AoA in the measurements is computed using the following procedure:

- Extract measured 1-minute averaged C_p^{exp} distributions for each blade section and bin average them on the flow angle measured directly by the pitot tube located at r/R=0.78 using bins of $\pm 0.5^o$, i.e. establish $C_p^{exp}(AoA_{pitot})$
- From the 3D rotor computations determine the AoA for each blade section using the AAT and establish the computed $C_p^{cfd}(AoA)$.
- Estimate the measured AoA in an optimization process involving minimizing the objective function:

$$min \left\| \sum_{i=1}^{n} \left(C_p^{exp}(AoA_{pitot}) - C_p^{cfd}(AoA) \right)^2 \right\|$$

  where $n = 64$ is the number of pressure taps along the aerofoil section.

In this way transfer functions from AoA_{pitot} to AoA in 3D is established. This procedure is valid because an initial comparison of full scale measurements and rotor CFD showed reasonably good agreement in the pressure distributions.

Figure 4.21-4.22 shows the normal force and tangential force coefficients, respectively integrated from the C_p distributions.
Generally, the agreement between 3D rotor computations and rotor measurements is good, however there are important differences at r/R=0.750, where it seems that C_n measured on the rotor is closer to the $2D$ computations.
At high AoA the C_n values indicate delay in stall at r/R=0.325 and r/R=0.475. At the outermost section the C_n values are below the 2D values for all AoA and it also seems that the slope of the C_n curve is lower in 3D than in 2D. Shen et al. [47] showed similar behaviour of the lift coefficient near the tip of a rotor.

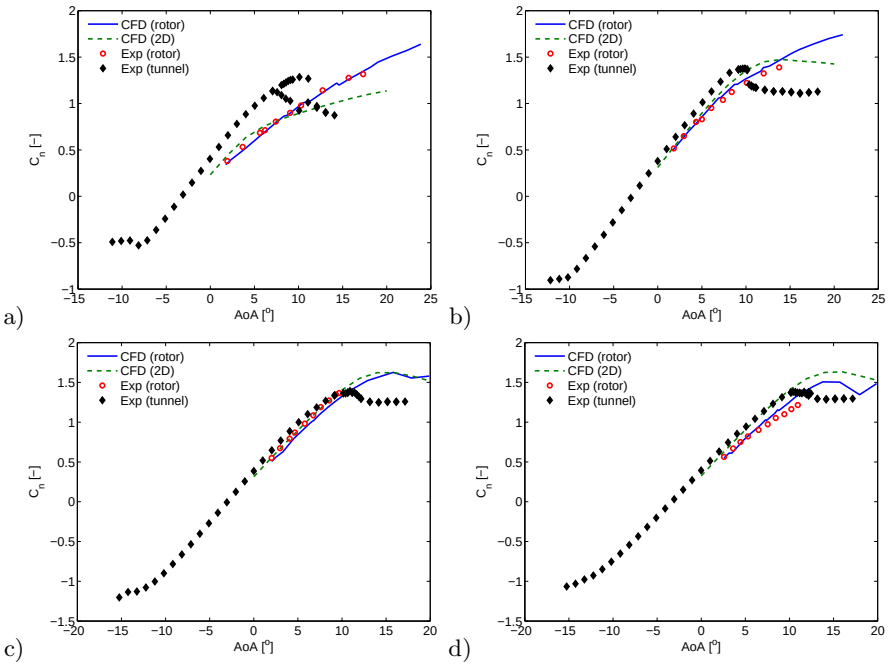

Figure 4.21: *C_n polars at a) r/R=0.325; b) r/R=0.475; c) r/R=0.750; d) r/R=0.925.*

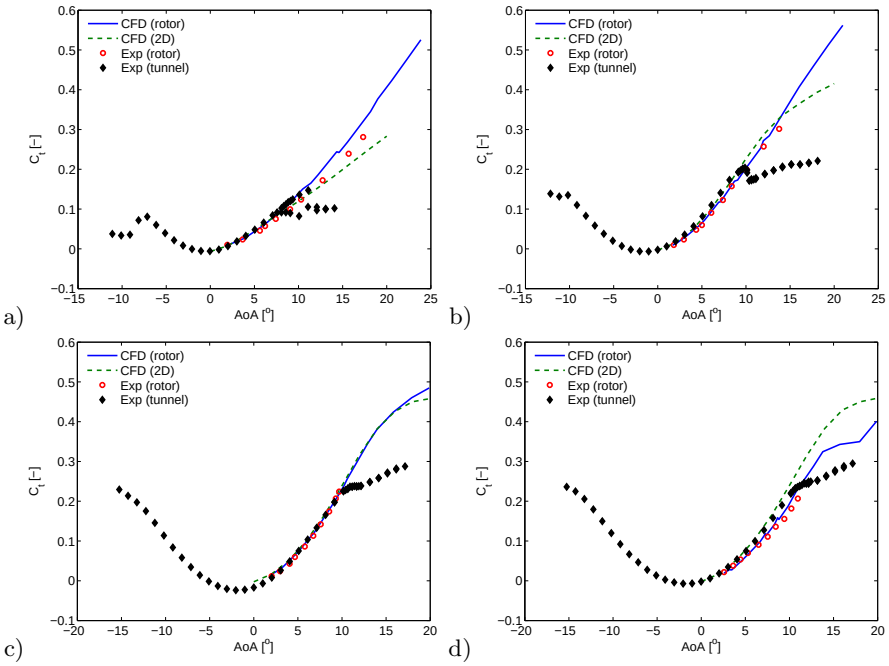

Figure 4.22: *C_t polars at a) r/R=0.325; b) r/R=0.475; c) r/R=0.750; d) r/R=0.925.*

4.3.2 Development and Validation of an Actuator Vortex Generator Model

The objective of this task is to develop and validate a CFD based vortex generator (VG) model, which uses body forces to represent the VG. The advantage of such a model is that there is no need for a mesh around the individual VG, which presents a large reduction in the computational expenses.

Actuator VG Model

The developed model is based on the actuator shape method and a modified version of the so-called BAY model. The basic idea behind the model is to let the VG be represented by a lift force which depends on the local flow conditions and the VG shape and is determined using an analogy to thin aerofoil theory, see Figure 4.23. The force applied to a given computational cell i is proportional to the area of the intersection

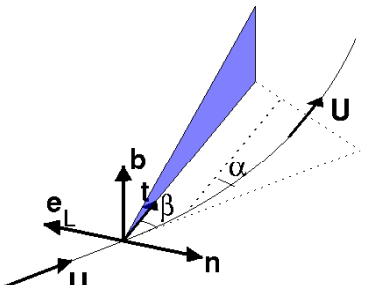

Figure 4.23: *Sketch of VG with definition of terms in the BAY model*

between the VG and the cell, i.e.

$$\mathbf{L}_i = C_{VG}\rho A_i |\mathbf{U}|^2 \alpha \mathbf{e}_L \tag{4.3}$$

where

$$\begin{aligned} \mathbf{e}_L &= \frac{\mathbf{U}\times\mathbf{b}}{|\mathbf{U}|} \\ \alpha &\approx \cos\alpha \sin\alpha = \frac{\mathbf{U}\cdot\mathbf{t}}{|\mathbf{U}|}\frac{\mathbf{U}\cdot\mathbf{n}}{|\mathbf{U}|} \end{aligned}$$

and A_i is the area of the intersection between cell i and the VG, whereas C_{VG} is calibration coefficient. If C_{VG} is set to a very high value the flow will be aligned with the VG ($\alpha \to 0$) and consequently $\mathbf{L}_i$ will be independent of C_{VG}.
The forces on the VGs are applied into the computational domain using the actuator shape model [34] and a modified Rhie-Chow algorithm [33] to avoid odd/even pressure decoupling. The model has been implemented into the in-house flow solver EllipSys3D.

Validation of the Model

The model is validated by applying it for modelling an array of VGs attached to the suction side of a FFA-W3-301 aerofoil section (see Figure 4.24) and compare it to wind tunnel measurements [46] and fully resolved (FR) CFD [40]. In the considered configuration the VGs are shaped as delta wings with $h = 0.01c$, $l = 0.038c$ and with their leading edge at $x = 0.2c$, where c denotes the chord of the aerofoil. The VGs are positioned in pairs in a counter rotating configuration with $\beta = \pm 15.5^o$, $\Delta 1 = 0.04c$ and $\Delta 2 = 0.05c$, see figure 4.24. In order to limit the computational requirements of the fully resolved (FR) CFD simulations, only one of the two vanes in a VG unit was simulated exploiting the geometrical symmetry of a VG unit. The grid used for the fully resolved CFD simulations has an O-mesh structure with $N_c = 448$ grid cells in the chordwise direction, $N_n = 128$ normal to the aerofoil and $N_s = 64$ in the spanwise direction.
Initial studies with the BAY model showed that for $C_{VG} > 1$, the simulation results are rather insensitive to C_{VG} and in the following $C_{VG} = 8$ is therefore used.
In order to establish the overall requirements for the grid when using the BAY model a grid sensitivity

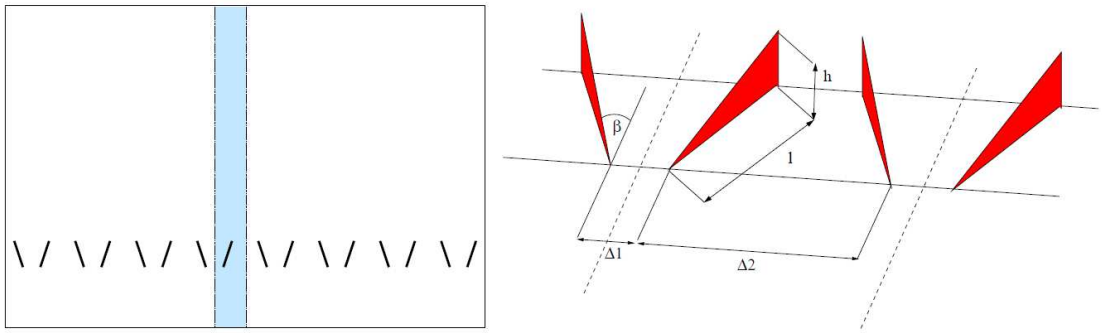

Figure 4.24: *Left: Top-down view of the aerofoil equipped with an array of VGs. The coloured region indicates the symmetry unit used in the computations and the incoming flow is from down. Right: A sketch defining the characteristic dimensions of the VG setup*

study was carried out. The study mainly focused on the sensitivity of the model to spanwise resolution. This was achieved by increasing the span, L_s, of the simulated aerofoil section and hence also the number of VGs, N_{VG}. The tested grid configurations are listed in Table 4.3, where G_0 represents the grid used for the FR simulation. Figure 4.25 compares the lift and drag curves obtained using the BAY model on

Grid	N_c	N_n	N_s	L_s/c	N_{VG}
G0	448	128	64	0.045	1
G1	256	128	32	0.045	1
G2	256	128	32	0.090	2
G3	256	128	32	0.180	4
G4	256	128	32	0.360	8

Table 4.3: Grid configurations used for the sensitivity study

different grids with the fully resolved results. As seen the BAY model predicts the lift quite accurately on all grids. On grid G4 the drag is seen to be slightly over predicted at high angles of attack, when compared to the predictions on the other grids. The simulated drag is seen to be underestimated on all grids in comparison with the measurements, which is most likely a consequence of not simulating the bed that the VGs are installed on in the experiment.
On grid G4 the number of grid cells is only 1/28 of the number of cells used in the FR computation and thus the BAY model proves to be able to reduce the number of cells significantly without compromising too much the accuracy of the lift and drag.

Grid Requirements for Simulating a Wind Turbine Equipped With VGs

In a standard CFD rotor simulation the number of grid points used to resolve a wind turbine blade is approximately $N_c = 256$, $N_n = 128$ and $N_s = 128$ which gives about $14 \cdot 10^6$ cells to resolve the entire rotor. The required number of grid points for simulating a rotor where the inboard span of the blade is equipped with a row of VGs can be estimated based on the above mesh study. Assume that about 30% of the blade span is equipped with VGs and that the average chord of the blade here is about $c = R/15$, i.e. the considered span has a length of $L_s = 4.5c$. In order to achieve a G4 grid resolution, the considered span should thus be resolved with $4.5/0.36 \cdot 32 = 400$ grid cells (corresponding to 50 VG pairs) and the entire blade span would require about 500 grid cells, i.e. $N_s = 500$. Assuming N_c and N_n to be unaltered then the total number of grid cells needed for simulating a typical wind turbine with a row of VGs would be about $50 \cdot 10^6$. Thus, simulating a rotor fitted with rows of VGs requires about 3.5 times more grid points than for a rotor without which is acceptable.

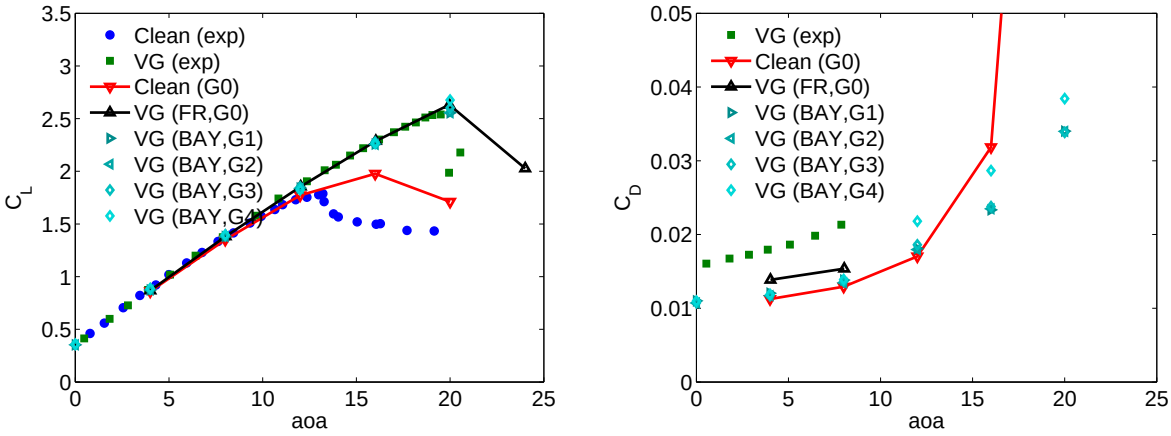

Figure 4.25: *Comparison of lift and drag curves for the FFA-W3-301 aerofoil with VGs obtained on different grids.*

4.3.3 Aerodynamic Analysis of a 10 MW Wind Turbine Using 3D CFD

This section describes a comprehensive aerodynamic analysis carried out on the DTU 10 MW Reference Wind Turbine [7] (DTU 10MW RWT), in which 3D CFD simulations were used to analyse the rotor performance and derive airfoil aerodynamic characteristics for use in aero-elastic simulation tools. A more detailed description of the work is given by Zahle et al. [49].

3D CFD Simulation Setup

All simulations were carried out using the incompressible Reynolds averaged Navier-Stokes flow solver EllipSys3D [27, 28, 39].
The simulations were carried out assuming a fully developed turbulent boundary layer on the blade surface using the $k-\omega$ SST model by Menter et al. [24].
The rotor surface mesh consisted of 256 cells in the chord-wise direction and 128 cells in the span-wise direction with a 64×64 cells tip cap on each blade tip. The volume mesh was of the O-O type and was grown away from the surface using 128 cells in the normal direction to form a sphere with a radius of approximately 20 rotor radii. To obtain a $y+$ of less than 2 the height of the first cell in the boundary layer was set to 2×10^{-6} m.

Derivation of Airfoil Data

The original BEM airfoil data was based on 2D CFD computations on airfoil cross sections with relative thicknesses of [0.48, 0.36, 0.30, 0.24].
In the present work, aerofoil data was derived from 3D CFD simulations using the azimuthal averaging technique (AAT), see e.g. Johansen et al [19]. In this technique the axial and tangential velocities are extracted in the flow field at a given radius at different axial locations over an annulus, averaged azimuthally and interpolated at the position of the rotor.
The airfoil data was computed with the rotor operating at 10 m/s at the design RPM of 8.06 by varying the pitch setting across the range [-32,32] deg. with increments of 4 deg. to obtain airfoil data over a wide range of angles of attack.
Figures 4.26 to 4.29 show the resulting airfoil data (3D CFD AAT) compared to the original 2D CFD data corrected for 3D effects using the models by Bak et al. [6], Snel et al. [38], Lindenburg [23], Chaviaropoulos and Hansen [13], Du and Selig [15], Dumitreschu et al. [16].

For the 24% airfoil, only minor corrections are made to the 2D data, and it can be observed that the AAT-based data is in very close agreement with 2D CFD for the lift, whereas the drag is predicted slightly higher. This may be due to the coarser mesh resolution used in the 3D CFD simulations, 256×128 cells

versus 768×256 used in the 2D CFD simulations. Also for the 30% airfoil data the datasets are in good agreement, although the model by Chaviaropoulos and Hansen stands out since it appears to capture the stall delay and resulting increase in lift in the post stall region best. For the 36% airfoil section the 3D CFD based data shows a decreasing lift curve slope in the range AOA = [5, 10] deg. and has no distinguishable stall. While none of the models predict a decreasing lift curve slope, again the model by Chaviaropoulos and Hansen captures the high angle of attack lift quite well. For the 48% airfoil the 3D CFD based data again has no distinguishable stall but also displays a shift of the lift curve towards higher C_{l0}; an effect which is not captured by either of the models.

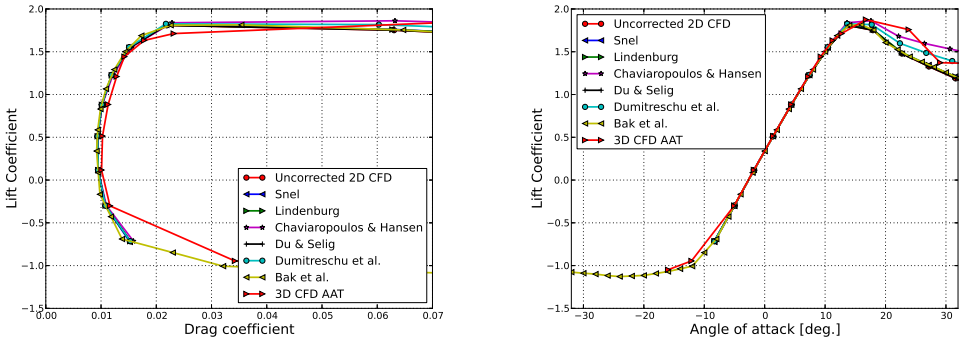

Figure 4.26: Lift and drag polars for the FFA-W3-241 airfoil (t/c= 0.24) at r/R = 0.785, based on 3D corrected airfoil simulations and 3D CFD, respectively.

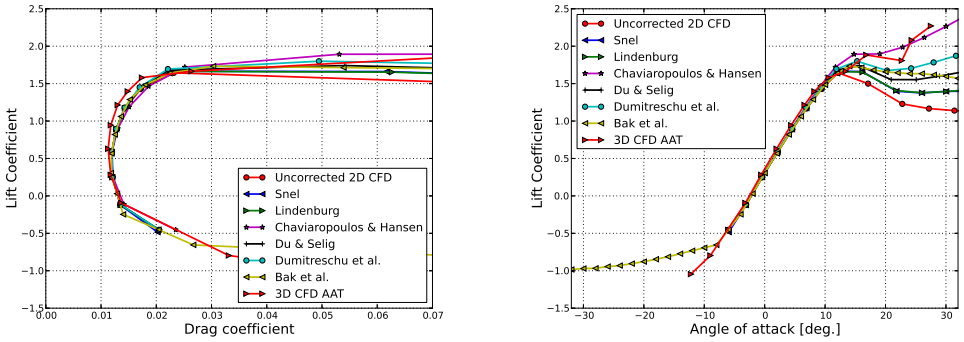

Figure 4.27: Lift and drag polars for the FFA-W3-301 airfoil (t/c= 0.301) at r/R = 0.408, based on 3D corrected airfoil simulations and 3D CFD, respectively.

Further understanding of the distinct deterioration in agreement between the engineering correction models and the AAT-based data for the inner part of the blade can be gained by investigating the flow state on the rotor surface. Figure 4.30 shows surface restricted streamlines on the rotor operating at 10 m/s. In the plot, the locations of the plotted airfoil data (t/c= [0.24, 0.30, 0.36, 0.47]) are indicated where it can be seen that the 3D radially pumped flow emanating from the root reaches out to the location of the 36% airfoil, whereas the flow at the location of the 30% airfoil is largely two-dimensional. This observation relates to one of the basic assumptions in many 3D correction models which is that they are only applied in the range of angles of attack where the 2D flow over an airfoil starts to separate. However, as is evident, the flow is permanently separated on this rotor for $r/R < .314$, where the relative thickness is greater than 36%, which cannot be accounted for in the engineering correction models.

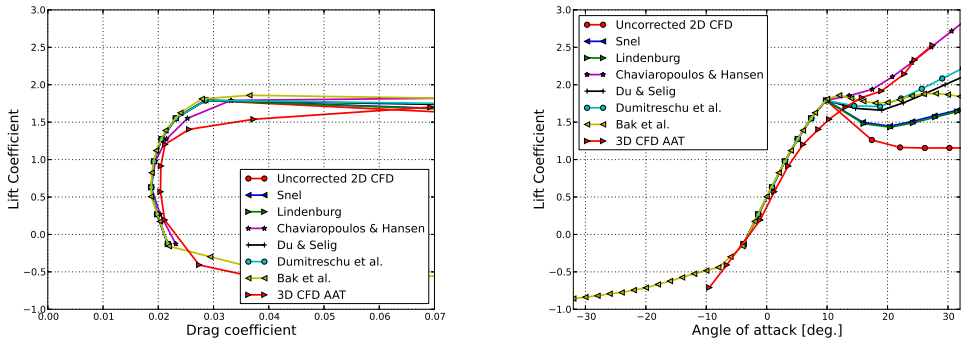

Figure 4.28: Lift and drag polars for the FFA-W3-360GF airfoil (t/c= 0.36) at r/R = 0.314, based on 3D corrected airfoil simulations and 3D CFD, respectively.

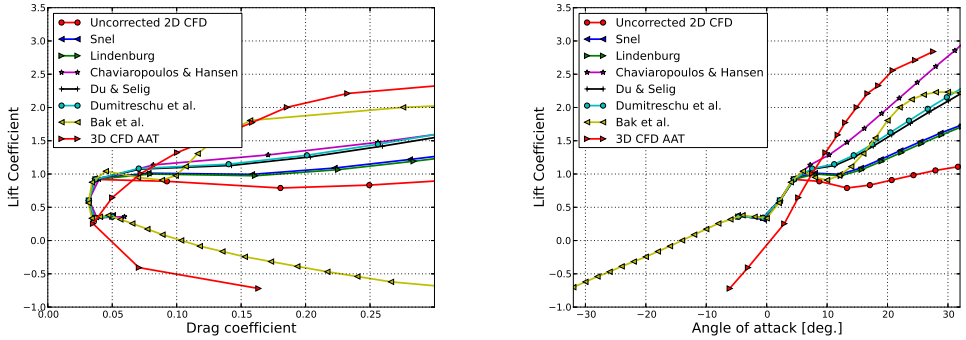

Figure 4.29: Lift and drag polars at r/R = 0.290 (t/c= 0.48), based on 3D corrected airfoil simulations and 3D CFD, respectively.

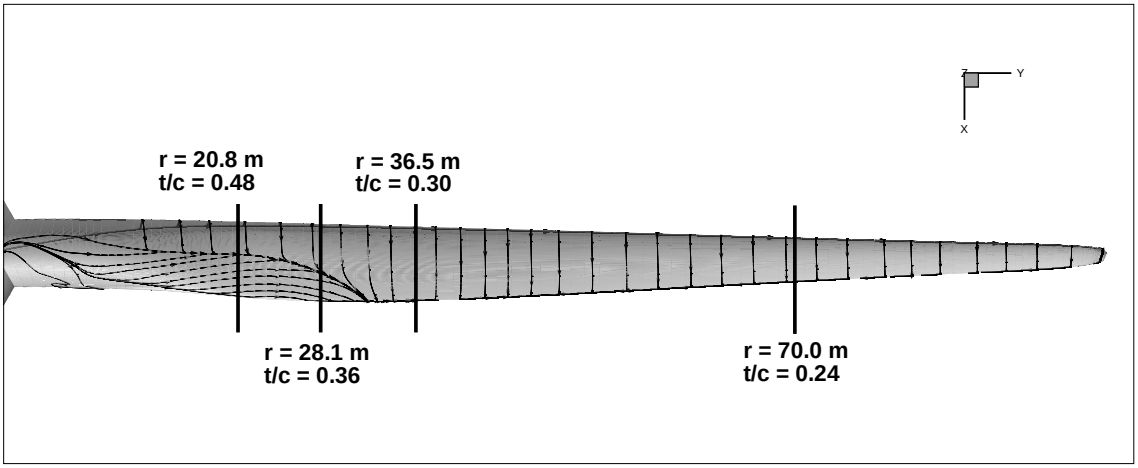

Figure 4.30: Surface restricted streamlines on the DTU 10MW RWT operating at 10 m/s, pitch = 0 deg. and RPM = 8.06.

Rotor Performance

To evaluate the 3D CFD based data BEM simulations were carried out using HAWC2 [22], comparing the original dataset based on 2D CFD with stall correction using the model by Bak et al. to the dataset based on 3D CFD both benchmarked against 3D CFD simulations at the exact same operational conditions. The chosen operating conditions were those used to derive the 3D CFD airfoil data with a wind speed of 10 m/s, a rotational speed of 8.06 RPM and a range of pitch angles. Since the 3D CFD based data is derived all the way to the tip, a tip-correction is not used in the BEM simulations for this dataset. Figure 4.31 shows the normal and tangential forces as function of span for three pitch angles [-4, 0, 4] deg., where 0 degrees pitch corresponds to the design point. Both BEM simulations agree quite well for 0 deg. and -4 deg. pitch, whereas they over-predict the normal force at the tip for the highly loaded case. The tangential force distribution predicted using BEM agrees quite well with the 3D CFD simulations, although the CFD results predict a consistently higher tangential force on the mid-part of the blade. For the 4 deg. pitch case, the agreement is quite poor towards the tip, where the CFD simulations predict a distinct drop in tangential force, which is not captured in either of the BEM simulations. Figure 4.32 show the mechanical

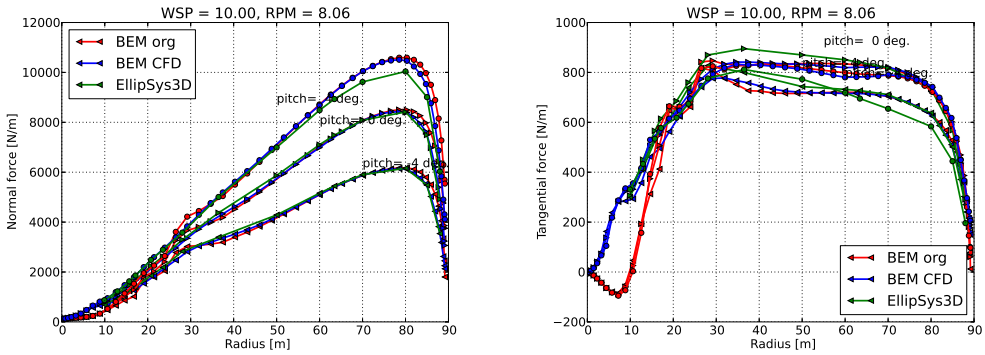

Figure 4.31: Lift and drag along the span of the blade for a range of pitch settings.

power and thrust as function of wind speed computed using EllipSys3D compared to BEM computations made using the original 2D CFD based airfoil dataset and the new 3D CFD based dataset all computed at the same operational conditions. While the detailed plots of the tangential and normal forces showed improved agreement between BEM and 3D CFD using 3D CFD based airfoil data, there is no significant improvements on the integrated power and thrust.

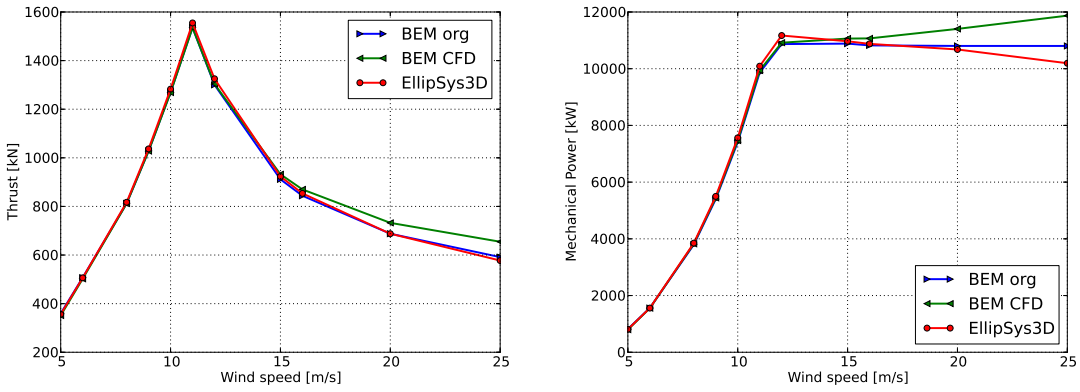

Figure 4.32: Power and thrust as function of wind speed for the rotor computed using EllipSys3D compared to HAWC2 simulations.

Conclusion

In this section a comprehensive 3D CFD study has been carried out on the DTU 10MW Reference Wind Turbine, in which airfoil data for use in BEM-based codes was derived using the Azimuthal Averaging Technique (AAT) using steady state rotor simulations. The derived airfoil data was used in the aeroelastic code HAWC2 to quantify whether the 3D CFD based data compares better to 3D CFD results than the original airfoil data, which is based on 2D CFD and 3D correction using the model by Bak et al. [6]. While comparisons of the spanwise distributed forces showed a clear improvement, particularly on the inner part of the blade, the resulting predicted mechanical power and thrust did not show significant improvements. This is, however, primarily due to the fact that the majority of both thrust and power production is produced on the outer part of the rotor, where the original dataset compares well with the 3D CFD results.

4.4 WP3: Identification of the Standstill Problem

Author(s): Witold Skrzypinski, Joachim Heinz, Frederik Zahle, Niels N. Sørensen

One of the challenges in the development of megawatt sized wind turbines is the presence of so called standstill vibrations of blades, i.e. vibrations which may only occur when the turbines are not in operation. Standstill vibrations may be experienced at newly erected turbines before they are connected to the grid, as well as at turbines which undergo maintenance, experience extreme wind conditions or breakdown. One of the characteristic features of the vibrations is that they may only occur at angles of attack significantly higher than those experienced in normal operation. Elimination of the vibrations may increase the lifetime of blades and decrease the number of incidents in which blades are damaged. Scientific work regarding blade vibrations at standstill conditions may benefit both the academia and the industry as only thorough understanding of the involved physics and the nature of vibrations may lead to accurate and efficient modelling of the vibrations and the development of the methods to mitigate their negative effects.

The present work comprised Computational Fluid Dynamics (CFD) computations, wind tunnel measurements as well as development of methods for an accurate and efficient estimation of 360 degrees polars which may be crucial for accurately modelling of standstill vibrations. Furthermore, CFD computations were carried out on extruded aerofoils without twist or taper, with non-moving, prescribed motion, and elastically mounted aerofoil suspensions. Computations on extruded aerofoils aimed at thoroughly understanding the basic physical phenomena governing the vibrations. None the less, extruded profiles without twist or taper are not necessarily representative of complex wind turbine blades. Therefore, computations on blades were carried out as well, incorporating an innovative coupling of CFD with an aeroelastic code. Finally, an attempt was made at modelling the vibrations. However, due to the complex nature of the physical phenomena, the work is still in progress and continued as part of another EUDP project.

4.4.1 Extraction of 360 Degrees Airfoil Data from CFD

This study describes a method to establish 360 degree airfoil data which is needed in aeroelastic codes to compute load cases outside normal operation[2]. Often this data is based on empirical formulae, however, as this study shows, the flow is highly unsteady and in mean not as smooth as standard empirical models predict. The aerofoil data created for the DTU 10MW RWT for angles of attack in the range AOA = [-180, -40] deg. and [40, 180] are based on simple empirical formulae:

$$C_l = 2 \cdot cos(AOA) \cdot sin(AOA) \tag{4.4}$$

$$C_d = c_{d,max} sin^2(AOA) \tag{4.5}$$

$$C_m = -sin(AOA)/4 \tag{4.6}$$

where $C_{d,max}$ is 1.5 at the outer part of the rotor based on results by Johansen et al. [20], i.e. for the aerofoil with 24% relative thickness, and 1.3 for the mid and inner part of the rotor.

In this work unsteady 3D CFD simulations were carried out on a single blade of the DTU 10MW RWT using the DES model by Menter. A time step of Δt=0.005 sec. was used, with a total time of 60 sec. after an initial simulation time to eliminate simulations transients. The averaged results presented in this work were averaged over a time window of 20 sec. A total of 36 simulations were carried out in the range [-180,180] deg. flow angle relative to the blade pointing into the wind at 0 deg. flow angle. Figure 4.33 shows plots of the flow structures in the wake of the blade with a wind direction of 140 deg. (corresponding approximately to AOA = -140 deg. relative to the local aerofoil coordinate system), visualized as an iso-surface of vorticity magnitude and contours of the y-component of vorticity in a y-plane at 60 m radius.

Figure 4.34 shows the lift, drag and moment coefficients, as function of the local blade section angle of attack (taking the blade twist into account) compared to the reference data computed using Equations 4.4 to 4.6. Note that the reference dataset is a merged dataset of operational aerofoil data for the range AOA = [-32,32] with standstill data. As such a comparison of the standstill CFD data should only be made outside of this range. The 3D CFD based data agrees well with the simplified model in the range AOA = -50 deg, whereas the predicted C_l at AOA = -135 and AOA = 135 deg is lower than that used in the simple model. Turning to the drag coefficient, the simulations do not predict a smooth sinusoidal curve,

[2]Partially reproduced from the article by Zahle et al. [49]

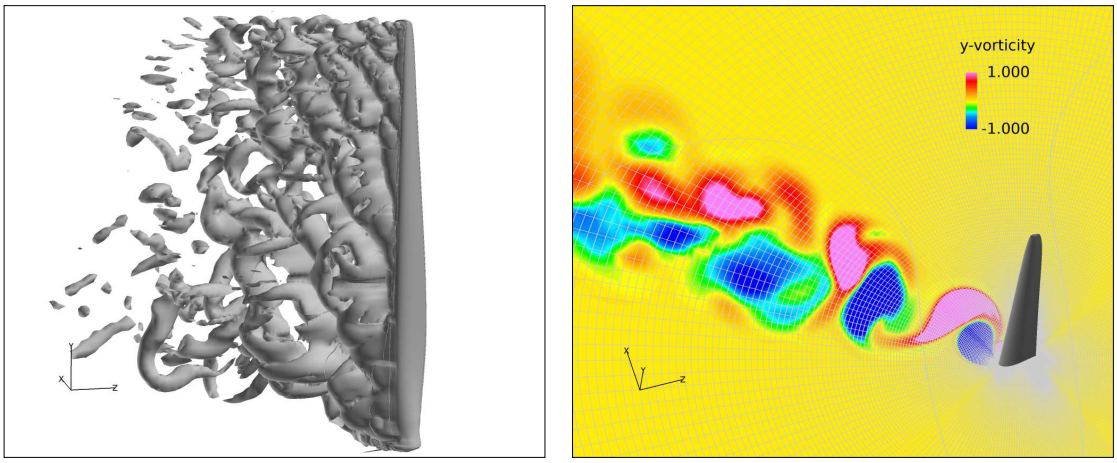

(a) (b)

Figure 4.33: Flow visualization of the DTU 10MW RWT blade at standstill at 12 m/s flow velocity and 140 deg flow angle. (a) Iso-surface of vorticity magnitude, (b) Contour surface at y=60 m showing the y-component of the vorticity.

but predict distinct peaks in C_d in the range AOA = [-140, -110], AOA = ±50 deg. and to some degree AOA = 140 deg. These peaks correspond to situations where the vortex shedding along the blade displays a high degree of spanwise correlation.

While the averaged CFD results derived for BEM codes do not contain any information on the unsteady content of the lift and drag, these simulations indicate at which flow conditions, spanwise correlation of the vortex shedding could be largest, possibly exciting the blade dynamically giving rise to standstill vibration. To investigate this, a coupled structural CFD solver with HAWC2 providing the structural deflections and EllipSys3D providing the aerodynamic loads has been developed, which is described in more detail in Section 4.4.5.

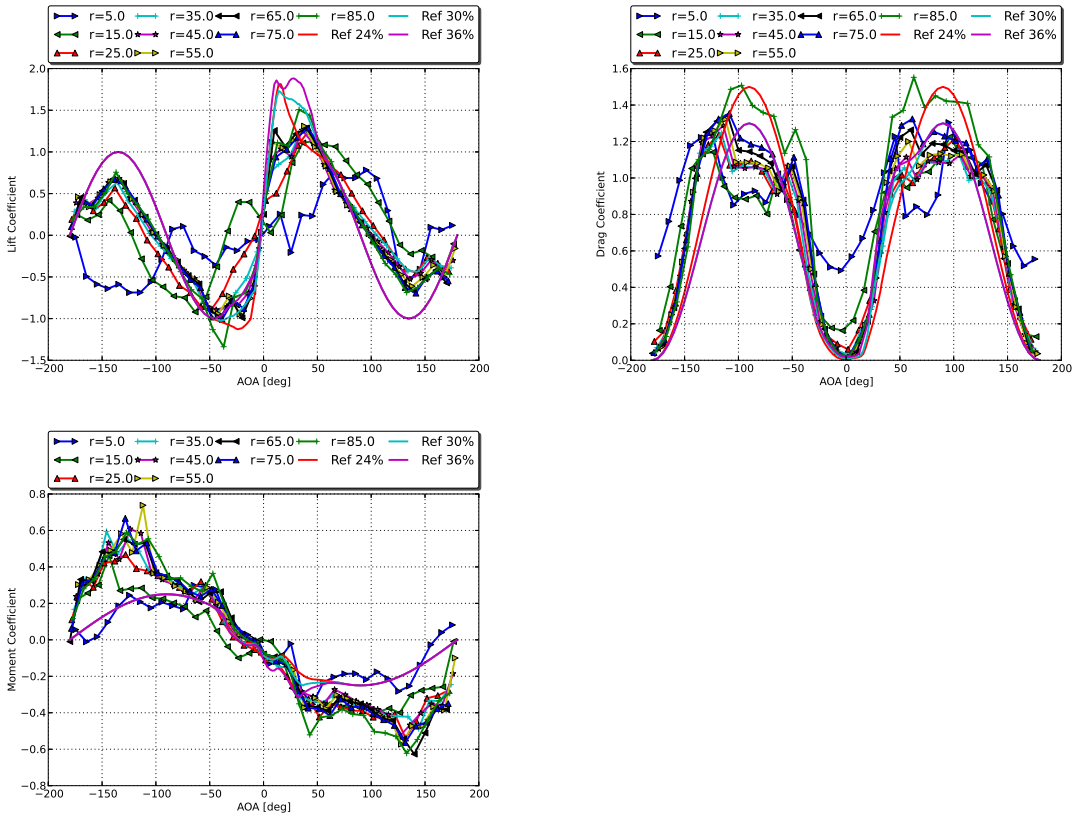

Figure 4.34: Lift, drag and moment coefficients as function of local angle of attack for the DTU 10MW RWT at standstill computed at 12 m/s wind speed.

4.4.2 Experimental Establishment of 360 Degree Aerofoil Polars

Author(s): Rolf Hansen (LM Wind Power)

During normal operation of the wind turbine, the polars measured at the LM LSWT between minimum and maximum stall are sufficient for predicting the power curve of the turbine. However when the turbine is in non-normal operation like shutdowns and emergency stops due to storms etc, the blades experience a wide range of angles of attack. Therefore it is important to know the full 360 degree polar. Measurement of a full 360 degree polar is very difficult in the LM LSWT due to the high blockage the airfoil model imposes at especially ±90 degrees. A DU-91-W2-250 airfoil with a chord of 900mm is in stock at LM LSWT. An exact copy of this airfoil with a chord of 600mm has therefore been manufactured in order to reduce the blockage at these angles with the aim to develop and validate mathematical wall corrections when doing a full 360 degree polar. The models have been tested and the results are shown below.

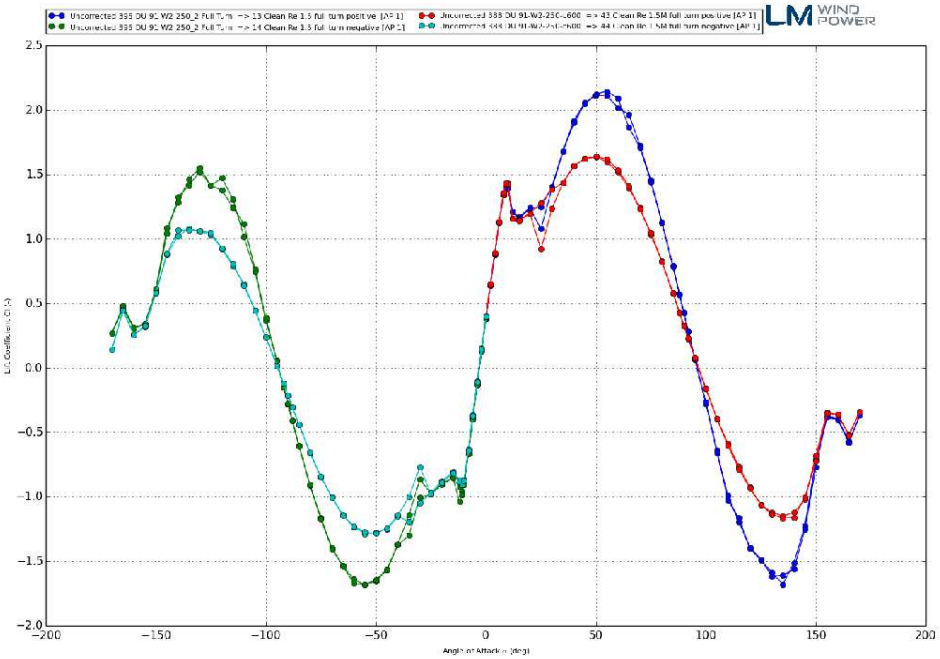

Figure 4.35: Full 360 degree lift polar with no wall corrections applied.

The non-wall corrected results show that as expected the lift is lower at the peaks, and that the drag at max blockage is also lower (±90 degrees) for the 600mm model. These results are crucial for LM for further development of valid wall corrections to account for the effect of confinement imposed by the walls. In the plot below the two aerofoils are shown in the linear range of the lift curve. The results show what is expected. Namely that they are very similar, but that the slope of the lift curve for the 600mm chord model is higher, due to a higher Ma number.

By applying a compressibility transformation onto the results to Ma number of 0.15 using the Prandtl-Glauert method, the lift slopes are almost identical.

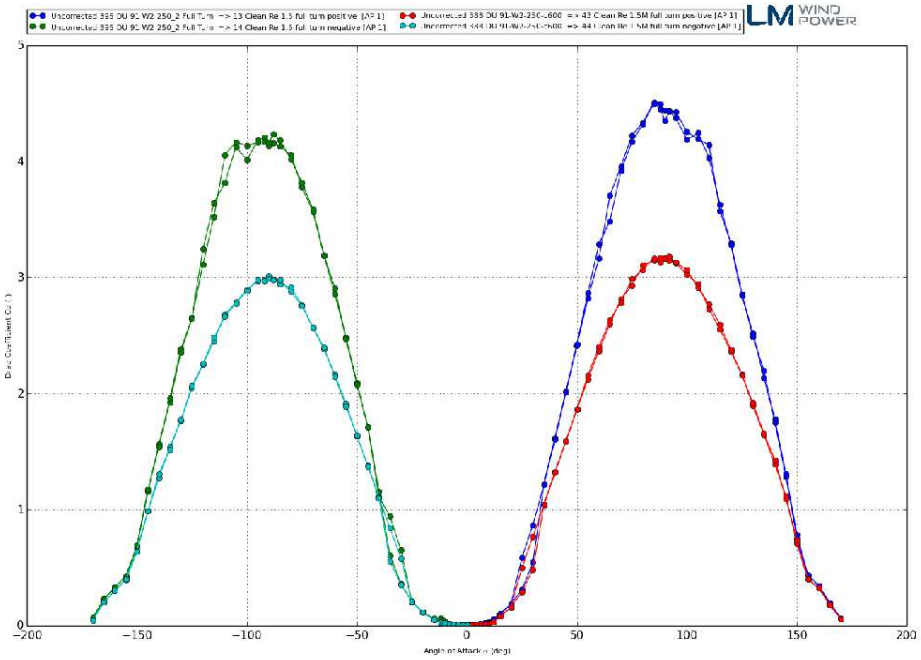

Figure 4.36: Full 360 degree drag polar with no wall corrections applied.

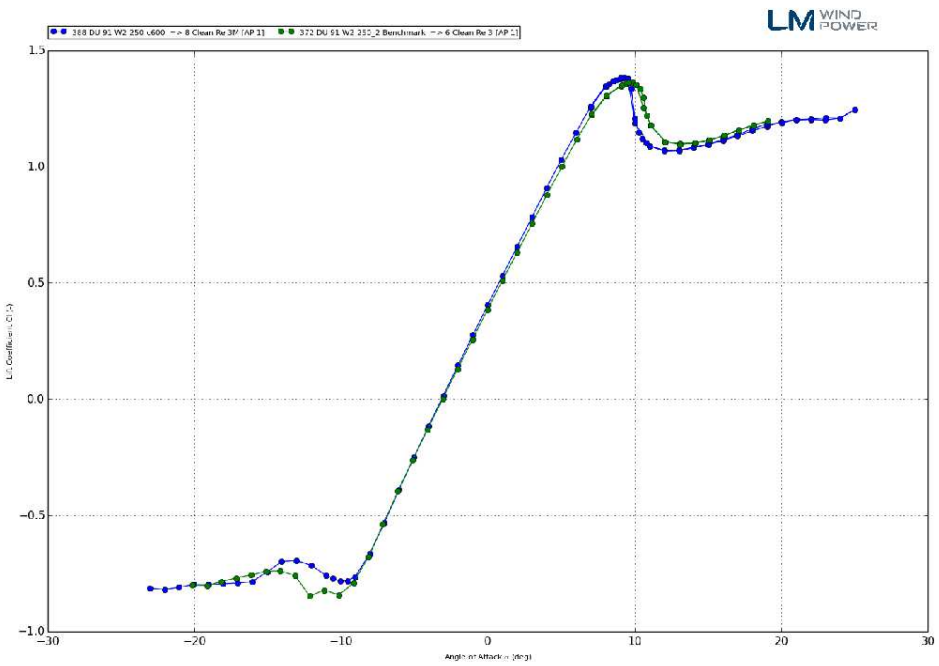

Figure 4.37: Comparison between 600mm model and 900mm model at Reynolds 3 million. Ma number for 600mm model is 0.225 and 0.15 for 900mm model.

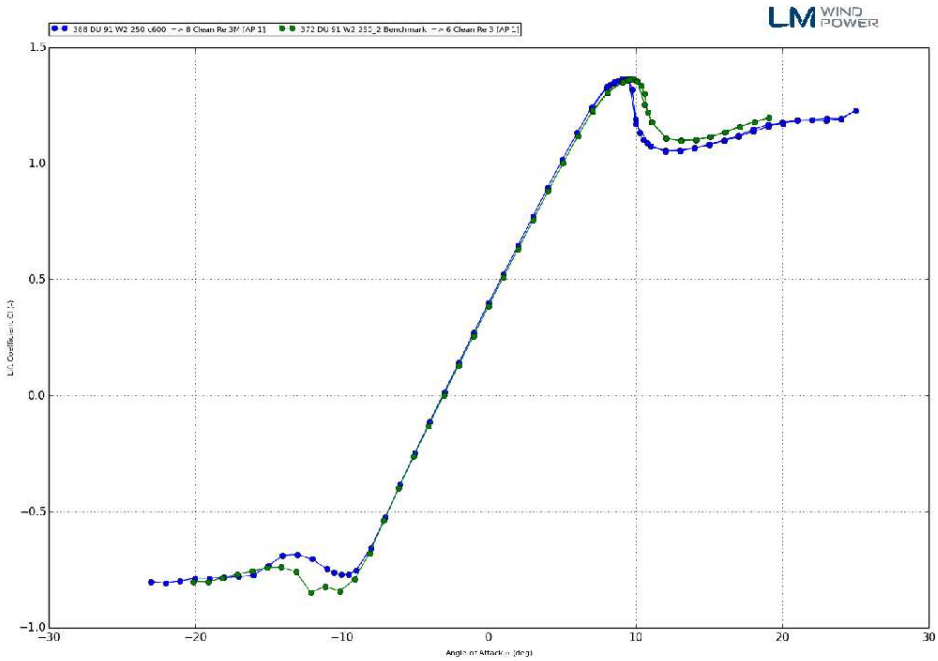

Figure 4.38: Comparison between 600mm model and 900mm model at Reynolds 3 million. Compressibility transformation applied to a Ma number of 0.15.

4.4.3 Development of an Engineering Model for Estimation of 360 Degrees Aerodynamic Coefficients

Every new turbine model undergoes certification prior to production. The certification process includes aeroelastic modelling which includes modelling at high angles of attack with the scope on standstill vibrations, for which accurate and efficient estimation of 360 degrees coefficients may be crucial.

Three different methods for estimating the aerodynamic characteristics at high angles of attack, some of which currently used in the industry, were analysed in the present work disseminated by Skrzypiński, Zahle and Bak [35]. One of those methods was further developed. The accuracy of the estimation, especially for chambered aerofoils, practically used on all megawatt sized wind turbines, was increased. In order to obtain an optimal balance between the accuracy and efficiency, it was also investigated to what extent relatively computationally inexpensive two-dimensional (2D) Computational Fluid Dynamics (CFD) computations may be used to aid the engineering modelling. This analysis indicated that the angle of attack region in the vicinity of 180 deg. may be computed using 2D CFD, apart from the normally computed in 2D CFD operational angle of attack region. An example of the application of the present work is presented in Figure 4.39, which shows a full 360 deg.lift coefficient curve.

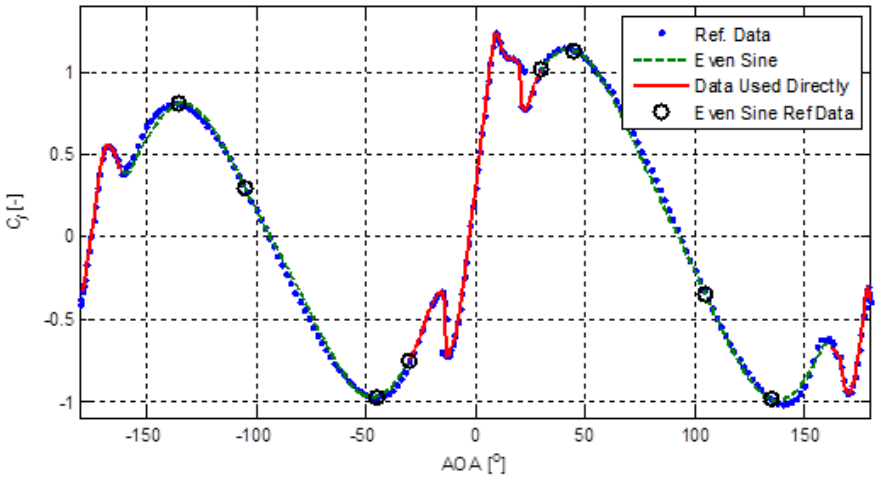

Figure 4.39: Approximation of the lift coefficient (Cl) at high values of the angle of attack (AOA), presented with the reference data, data used directly, and data points used to tune the present model; figure reproduced from [35].

The approximation is plotted with the dashed green line. The solid red line represents the 2D CFD data used directly. The blue dotted line represents the reference whereas the black circles represent the data used to tune the model. The result of the estimation was satisfactory, among other characteristics, reflecting the different maxima at positive and negative angle of attack regions. Judging by the results, it appears that the objective of the project task was realized.

4.4.4 3D Aeroelastic CFD on a Blade Section

Wind turbine blade vibrations at standstill conditions are potentially related to two separate physical phenomena: vortex-induced vibrations (VIV) and stall-induced vibrations (SIV). Thorough understanding of each phenomenon in the context of wind turbine blades is crucial for the ability to accurately model standstill vibrations and incorporate methods to eliminate them. Elimination of the vibrations may increase the lifetime of blades and decrease the number of incidents in which blades are damaged. In VIV, the blade vibrates given that at a relatively high angle of attack the wind speed is such that the associated frequency of vortex shedding, depicted in Figure 4.40, coincides with the natural frequency of the first edgewise mode. The present work, disseminated by Skrzypiński et al. [36], included the analysis of VIVs of an extruded aerofoil at 90 degrees angle of attack, based on 2D and 3D CFD computations with non-moving, prescribed motion, and elastically mounted aerofoil suspensions. The aerofoil was neither twisted nor tapered. It was found that the stationary vortex-shedding frequencies computed in 2D and 3D CFD differed. In the prescribed motion computations, the aerofoil oscillated in the direction of the chord line (horizontal). Negative aerodynamic damping indicating the presence of vibrations, found in both 2D and 3D CFD computations with moving aerofoil, appeared in the vicinity of the stationary vortex shedding frequency computed by 2D CFD. In general, the results indicated that even though 2D CFD computations seem to be capable of indicating the presence of vortex-induced vibrations at 90 deg. angle of attack, 3D CFD computations reflect the involved physics more accurately.

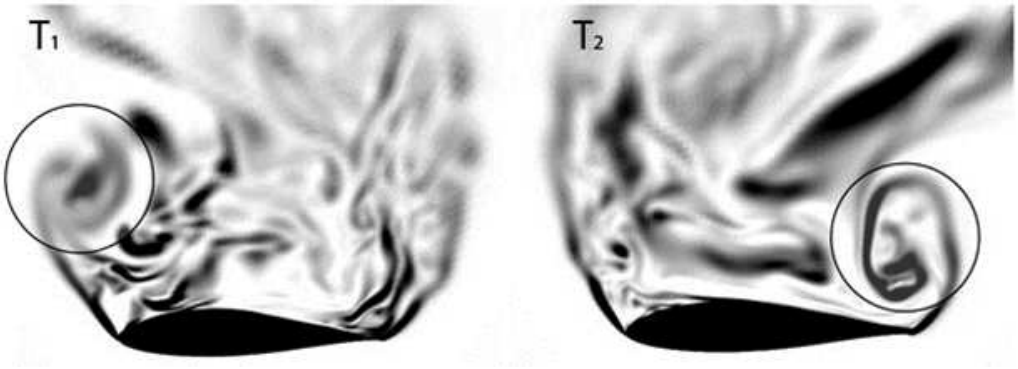

Figure 4.40: Snapshots presenting vorticity magnitude of the 3D flow around a section of an extruded airfoil extracted from CFD computations; presenting vortices shed from the leading and trailing edges of the airfoil; reproduced from [36].

In SIV – often referred to as galloping, stall flutter or bluff-body flutter – a small displacement of the body causes an increase in the aerodynamic force in the direction of its motion, resulting in the negative aerodynamic damping, and thus vibrations. The classic example of SIV is vibration of ice-coated power lines. The present work, disseminated by Skrzypiński et al. [36], included the analysis of both VIVs and SIVs of an extruded aerofoil based on 2D and 3D CFD computations with non-moving, prescribed motion, and elastically mounted aerofoil suspensions. Again, the aerofoil was neither twisted nor tapered. The aerofoil was analysed in the angle of attack region potentially corresponding to stall-induced vibrations, i.e. in the vicinity of 25 degrees angle of attack. The analysis showed fundamental and significant differences between the aerodynamic stability limits predicted by 2D and 3D CFD in this angle of attack region which is presented in Figure 4.41. The dimensionless power (P^*) on the y axis indicates the presence of vibrations if its value is positive. The dimensionless time period (T^*) is actually representative of the wind speed. The difference between the curves representing 2D and 3D CFD is clearly visible.

A general agreement was reached between the prescribed motion and elastically mounted aerofoil computations. 3D computations indicated that VIVs are likely to occur at modern wind turbine blades at standstill conditions. In contrast, the cut-in wind speed predicted by 3D CFD necessary for the onset of SIVs appeared high enough for such vibrations to be unlikely. To be more specific, assuming that the chord length of the blade section was 2m and the frequency of the first edgewise mode 1Hz, a wind speed in the range of 90 m/s would be necessary for the SIVs to occur. This is presented in Figure 4.42 where P^* assumes positive values on the left and right hand sides of the figure. The former represents VIVs whereas the latter represents SIVs. The T^* value of 45 where the P^* assumes the positive value corresponds to the

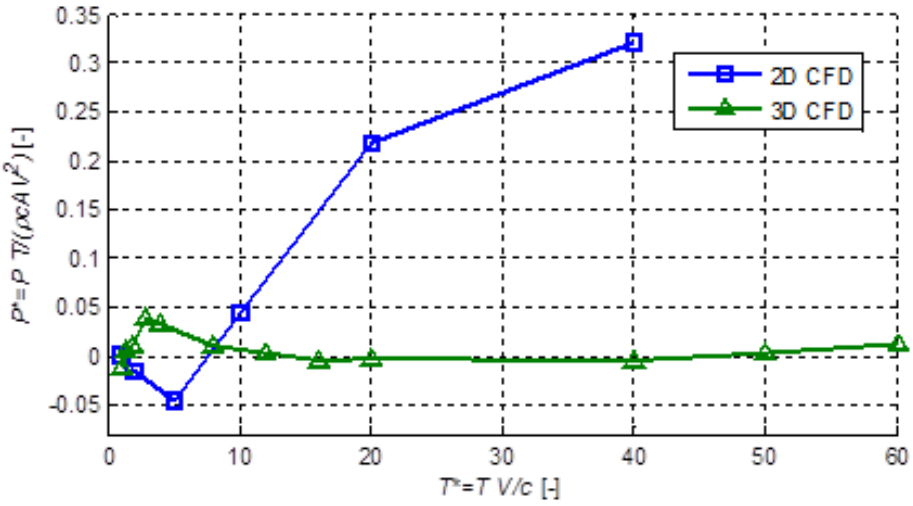

Figure 4.41: Dimensionless power (positive indicates vibrations) related to prescribed motion 2D and 3D CFD simulations of an airfoil; reproduced from [37].

aforementioned wind speed of approximately 90 m/s whereas the reference vertical red line corresponds to the wind speed of 50 m/s.

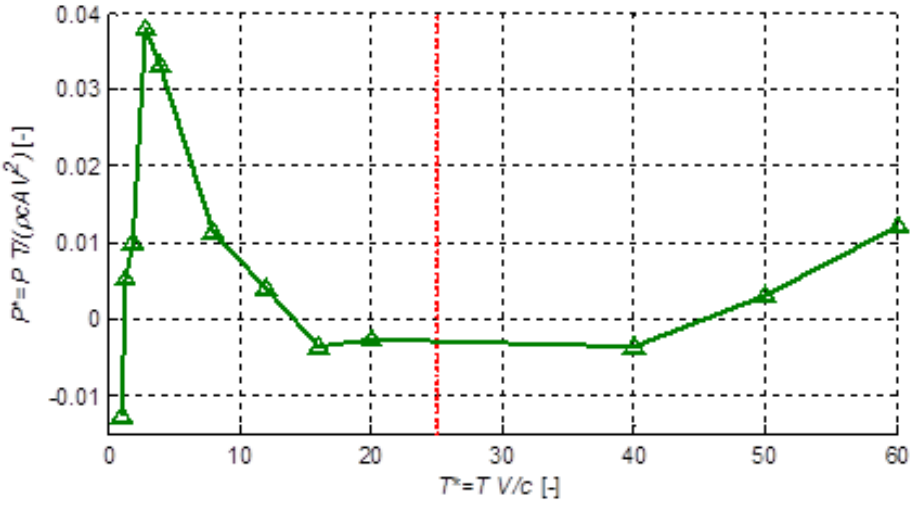

Figure 4.42: Dimensionless power (positive indicates vibrations) related to prescribed motion 3D CFD simulations of an airfoil; reproduced from [37].

Given the presented results, one may conclude that the objectives of the task were realized. Note that the aforementioned results were obtained using a non-twisted and non-tapered extruded aerofoil section in order to gain understanding of the governing phenomena. On the other hand, such an aerofoil is not necessarily representative of a more complex blade. Therefore, validation should be done by computations on blades, and preferably by utilizing the tools for the elastic CFD computations presented later in this report.

4.4.5 3D aeroelastic CFD on a Modern Wind Turbine Blade

The content of this section is mainly extracted from the pre-print of the submitted Wind Energy Journal Article of Joachim Heinz et. al [18]

Introduction

Within the field of wind energy the recent studies by Skrzypiński [36] and Zou [50] provide valuable knowledge in terms of vortex-induced vibrations on airfoils. They e.g. investigate the Strouhal number dependencies on airfoil shape, angle of attack and Reynolds number and examine the lock-in phenomena on an elastically mounted blade section. While Zou utilizes a two-dimensional vortex code and exclusively deals with vortex-induced vibrations on two dimensional airfoil sections Skrzypiński utilizes both two-dimensional and three-dimensional CFD computations on two-dimensional and three-dimensional extruded airfoil sections and employs both pure Reynolds averaged Navier Stokes (RANS) and Detached Eddy Simulation (DES) computations. Skrzypiński observed several differences between the two-dimensional and three-dimensional computations, especially when DES was used. However, the three-dimensional computations on the extruded airfoil section did not consider any blade twist or blade taper and the respective aero-elastic computations utilized a simple structural model with three degrees of freedom only. Those simplification made it still very difficult to come up with substantial predictions about possible vortex-induced vibration on a realistic wind turbine blade.
With the recently developed high-fidelity Fluid-Structure Interaction (FSI) simulation tool HAWC2CFD [17] it is now possible to investigate the standstill problem for a geometrically fully resolved wind turbine blade with realistic structural properties and three-dimensional high-fidelity CFD computations. The study can thus give a valuable contribution to the ongoing investigations of standstill blade vibrations.

The present work investigates the aero-elastic response of the DTU 10MW RWT blade [7] in standstill conditions. For the studied test cases the wind turbine blade is modelled on a fixed ground with the blade tip pointing upwards, similar to the blade illustrated in Figure 4.44d. Different inflow conditions are simulated by adjusting the wind speeds and inclining the inflow directions respectively to the CFD mesh. The utilized mesh exhibits 128 cells in the spanwise direction, 256 cells in the chordwise direction and 192 cells into the normal direction of the blade surface. The CFD computations are modelled without inflow turbulence. The influence of a turbulent inflow on the observed blade vibrations is thus not a subject of the current investigations.
The presented study focuses on angles of attack in the vicinity of 90 degrees. Under these angles of attack the shed vorticity results in an oscillating force which mainly acts in the edgewise direction and therefore mainly triggers edgewise vibrations. The work further focuses on relatively low to moderate windspeeds which generate vortex shedding frequencies in the vicinity of the first edgewise eigenfrequency of the blade. All observed and reported vibrations in the subsequent results section are thus vibrations of the first edgewise vibration mode of the DTU 10MW RWT blade.

Results

In order to better understand the complex aerodynamics and vortex shedding mechanisms behind a modern wind turbine blade at high angles of attack it was decided to begin the investigations by examining the flow behind an infinitely stiff blade structure. In this way the aerodynamics can be studied independently, without being influenced by an eventual blade motion. In a first test case the infinitely stiff blade of the DTU 10MW RWT is modelled during three different inflow conditions. The evolving vortex structure behind the blade was then analysed by evaluating the extracted force signals at various blade sections. For all tested inflow conditions of the stiff blade simulation setup the angles of attack at the various blade sections stay constant and exhibit $\mathrm{AOA_{tip}} = 90\,^\circ$ at blade sections close to the blade tip and, due to the structural pitch, $\mathrm{AOA}_{root} = 72\,^\circ$ at blade sections close to the blade root. The structural pitch as well as the chord length distribution of the DTU 10MW RWT blade are given in Figure 4.43a.
In previous investigations of the standstill problem such as in Skrzypiński [36] it was confirmed that the vortex shedding frequency f_v of an aerofoil section under angles of attack close to 90 degrees can be estimated with

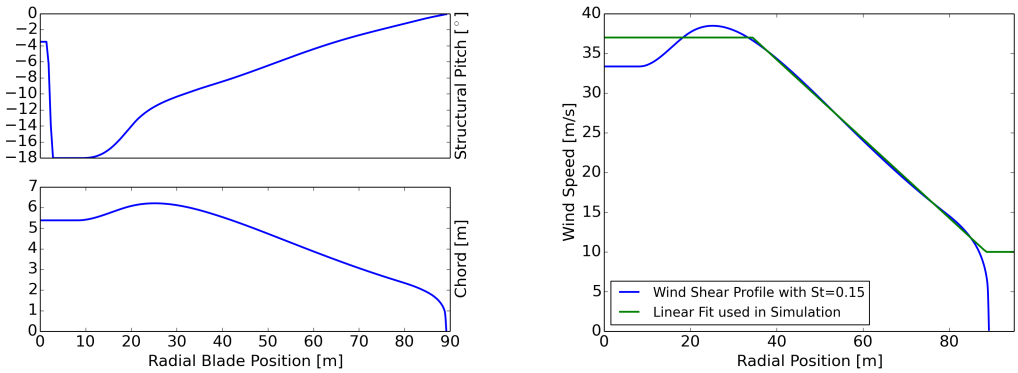

(a) Structural Pitch and Chord of DTU 10MW RWT blade

(b) Wind Shear Profile to trigger Vortex Shedding of 0.93Hz

Figure 4.43: Blade Properties and Wind Shear Profile

$$f_v = \frac{St \cdot V}{c} \tag{4.7}$$

with c being the projected chord of the aerofoil, V being the freestream velocity and St being the respective Strouhal number. Skrzypiński calculated the Strouhal numbers of a spanwise extruded DU96-W-180 aerofoil section with both RANS and DES computations and different spanwise extrusion lengths. The computations were conducted at a Reynolds number of $Re = 2 \cdot 10^6$ and the found Strouhal numbers varied from $St = 0.13$ for the shortest airfoil section computed with RANS to $St = 0.16$ for the longest airfoil section computed with DES. The obtained results could be interpreted as a gradual convergence towards a Strouhal number of $St = 0.17$ which was found by Chen and Fang in their experiments with a flat plate for various, but lower Reynolds numbers [14].
For a given Strouhal number Equation 4.7 can be used to generate a customized velocity profile in order to obtain the same vortex shedding frequency f_v along the entire blade of varying chord lengths. Figure 4.43b shows such a customized velocity profile for an assumed Strouhal number of $St = 0.15$ which adjusts the vortex shedding frequency to $f_v = 0.93\,Hz$ along the entire blade. This frequency is identical to the first edgewise vibration frequency of the investigated DTU 10MW RWT blade. A simulation with the respective velocity profile and a subsequent frequency analysis were carried out in order to evaluate the frequency content of the force variations in edgewise direction due to the highly unsteady aerodynamics. The results are illustrated in Figure 4.44a and clearly indicate a dominating frequency close to $0.93\,Hz$. The highest force intensities are found at blade sections with relatively long chord lengths at radial position of $r \leq 69\,m$, however, the lower force intensities at the outer blade sections might also add a decisive contribution to eventual blade vibrations in case a blade with realistic stiffness properties is considered.
For the customized wind shear profile of Figure 4.43b the wind speed at the blade root is more than $20\,m/s$ lower than at the blade tip and is thus describing a wind condition which is rather unlikely to occur. It is therefore interesting to also investigate some rather simple and more probable wind conditions. In Figure 4.44b the frequency analysis of a simulation with a uniform inflow of $V = 22\,m/s$ is shown. It can be seen that the spectra of the various blade sections are more diverse and exhibit peaks at different frequencies. At a radial blade position of $r = 59\,m$ the analysis indicates a pronounced peak at a frequency close to $0.93\,Hz$. Towards the blade tip, with blade sections of smaller chord lengths, the analysis reveals gradually higher vortex shedding frequencies. The findings thus confirm the validity of equation 4.7 but also indicate that the vortex shedding behind the blade is rather uncorrelated.
However, the lack of correlation starts vanishing when the inclination angle Ψ, as illustrated in Figure 4.44d, increases. For a simulation with the same uniform inflow velocity of $V = 22\,m/s$ but with an additional inclination angle of $\Psi = 25\,^\circ$ the respective frequency analysis of Figure 4.44c reveals again a coherent vortex shedding over large parts of the blade. The plot shows a pronounced peak at a frequency of approximately $1.00\,Hz$ comprising blade sections from $r = 59\,m$ to $r = 74\,m$. The increased correlation is obviously triggered by vortices that are shed at the outer part of the blade and then convected towards the inner part of the blade where they impose a vortex shedding of the same frequency. Utilizing equation 4.7 with a given vortex shedding frequency of $f_v = 1.00Hz$, an estimated Strouhal number of $St = 0.15$

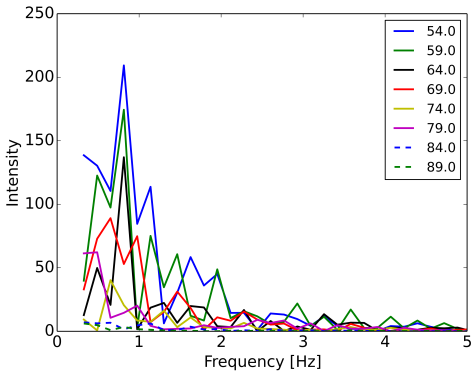

(a) Spectrum using Wind Shear Profile, $\text{AOA}_{\text{tip}} = 90\,°$, $\text{AOA}_{\text{root}} = 72\,°$, $\mathbf{\Psi} = 0\,°$

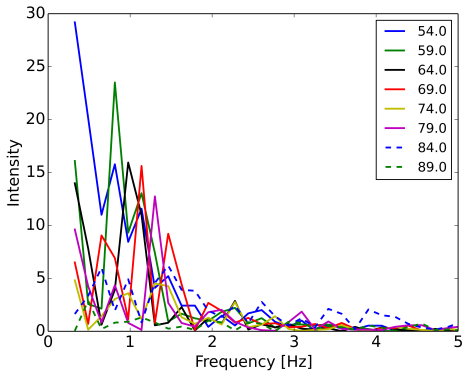

(b) Spectrum using Constant Inflow of 22m/s, $\text{AOA}_{\text{tip}} = 90\,°$, $\text{AOA}_{\text{root}} = 72\,°$, $\mathbf{\Psi} = 0\,°$

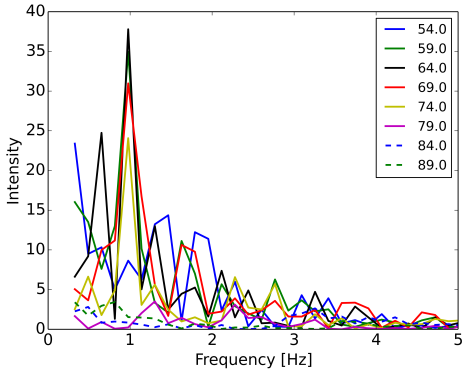

(c) Spectrum using Constant Inflow of 22m/s, $\text{AOA}_{\text{tip}} = 90\,°$, $\text{AOA}_{\text{root}} = 72\,°$, $\mathbf{\Psi} = 25\,°$

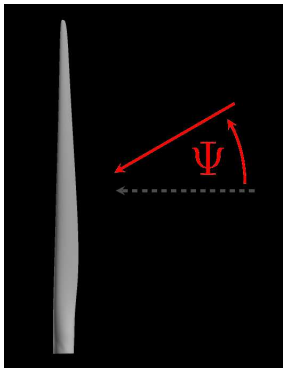

(d) Definition of Inflow Inclination Angle $\mathbf{\Psi}$

Figure 4.44: Frequency Spectra of Edgewise Forcing (Stiff Blade) and Inflow Inclination Angle $\mathbf{\Psi}$

and a projected inflow velocity of $V = V \cdot cos(\Psi) = 19.94\,m/s$ results in a chord length of $c = 2.99\,m$, which, on the investigated DTU 10MW RWT blade, is found at a radial blade position of $r = 71\,m$. This finding is in agreement with the observations of Figure 4.44c concluding that the vortices shed at this outer blade radius are convected towards the blade root and dictate the vortex shedding frequency on the inner parts of the blade as well. It seems that the flow conditions at the outer part of the blade are thus decisive for the generated vortex structures behind the entire blade. For negative inclination angles Ψ the inner parts of the blade would become more determative. However, due to the large chord lengths at the root much higher wind speeds would be needed in order to trigger critical shedding frequencies close to $0.93\,Hz$.

Despite those findings it is still considered difficult to utilize the frequency analysis of a stiff blade in order to identify the critical inflow conditions that trigger standstill vibrations. It is considered difficult to know how large the regions of correlated vortex shedding have to be, where these regions have to be located on the blade, which vortex shedding frequencies are close enough to create a lock-in with the respective structural vibration mode, how strong the oscillating forces need to be in order to put the blade in motion and, most importantly, it is considered difficult to then estimate how severe the resulting vibrations would be in amplitude. Since the computational time of an aero-elastic computation with HAWC2CFD is practically the same as a respective computation with a stiff structure it was therefore decided to directly conduct a comprehensive aero-elastic study for various inflow conditions in order to better define a range of critical wind conditions and directly quantify the respective aero-elastic responses.

The stiffness properties of the DTU 10MW RWT blade are now set to realistic values as given in [7] in order to conduct truly aero-elastic computations with HAWC2CFD. In a first aero-elastic test series different

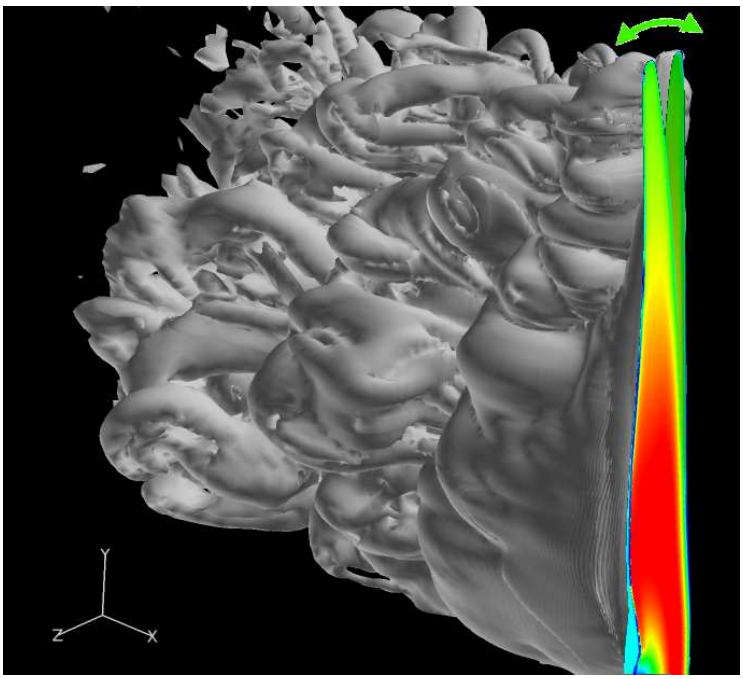

Figure 4.45: Aero-elastic Computations of the DTU 10MW RWT blade in Standstill

wind shear profiles of various Strouhal numbers are applied on the structure. The profile of Figure 4.43b shows a profile with an assumed Strouhal number of $St = 0.15$, however, considering Equation 4.7 and the previously mentioned range of Strouhal numbers found in the investigations of Skrzypiński [36] it is also interesting to see how the aero-elastic response changes for wind shear profiles of different Strouhal numbers. Figure 4.46a shows the maximum edgewise peak-to-peak amplitudes of the blade tip after a total simulation time of $T = 45\,s$. The style of the data point markers give information about the vibration type. An arrow to the left indicates that the maximum blade tip vibration amplitude was detected during the first time interval of $t \leq 20\,s$, an arrow pointing upwards indicates that the maximum was detected during the time interval of $20\,s \leq t \leq 35\,s$, an arrow to the right indicates that the maximum occured within $35\,s \leq t \leq 45\,s$, and a star indicates that the vibration was still in the process of further amplification when the simulation stopped at time $t = 45\,s$. Figure 4.46a shows computations of two different pitch settings corresponding to angles of attack at the blade tip of $\mathrm{AOA_{tip}} = 90\,^\circ$ for the red curve and $\mathrm{AOA_{tip}} = 100\,^\circ$ for the blue curve. It should be mentioned here that the given angles of attack are only constant while the blade is not vibrating. The computations show that the more severe edgewise vibrations occur for the pitch angle which corresponds to an angle of attack of $\mathrm{AOA_{tip}} = 100\,^\circ$. The highest amplitudes of the conducted test series can be found for $\mathrm{AOA_{tip}} = 100\,^\circ$ and a Strouhal number of $St = 0.15$. After 45 seconds of simulation the vibrations reach a peak-to-peak maximum of 8 meters which, in reality, would probably lead to an immediate blade failure. However, it should be remembered that the given wind shear profiles with wind speed differences between blade root and blade tip of more then $20\,m/s$ are rather unlikely to occur. The Figure also shows that for both investigated pitch angles the most severe vibration cases occur for Stouhal numbers close to $St = 0.15$. This is a strong indication that a Strouhal number of $St = 0.15$ is a very good guess for the investigated DTU 10MW RWT blade. Figure 4.45 shows a snap shot of a simulated vibration case when a customized wind shear profile with a Strouhal number of $St = 0.15$ is applied to the blade with an angle of attack at the tip of $\mathrm{AOA_{tip}} = 90\,^\circ$.

In contrast to the previously discussed simulations of various customized wind shear profiles, Figure 4.46b to Figure 4.47d show peak-to-peak amplitudes of simulations with wind conditions of uniform and inclined inflow which can definitely be considered realistic. The figures show simulations for seven different pitch angles using pitch steps of $5\,^\circ$ between each figure. The different blade pitch angles are used in order to vary the investigated angles of attack at the blade. To better identify the chosen pitch angles the corresponding angles of attack at blade tip and blade root are indicated below the figures. The results comprise angles from $\mathrm{AOA_{tip}} = 110\,^\circ$ to $\mathrm{AOA_{tip}} = 80\,^\circ$ and $\mathrm{AOA_{root}} = 92\,^\circ$ to $\mathrm{AOA_{root}} = 62\,^\circ$ respectively. Each figure

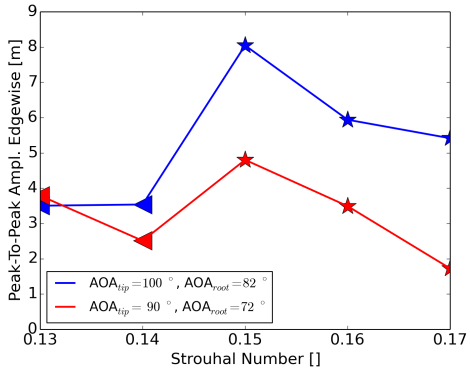

(a) Peak-to-Peak Ampl. using Wind Shear Profiles of Various Strouhal Numbers, Two Different Pitch Angles

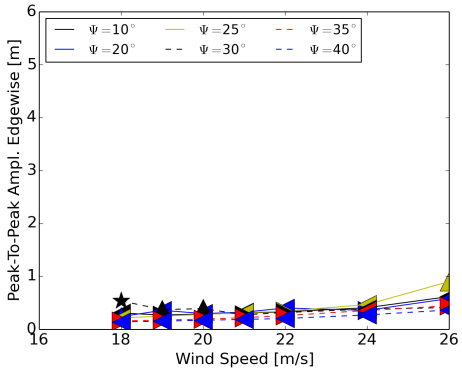

(b) $\mathrm{AOA_{tip}} = 110\,°$, $\mathrm{AOA_{root}} = 92\,°$ (Fixed Pitch), Uniform Inflow, Various Inclination Angles Ψ

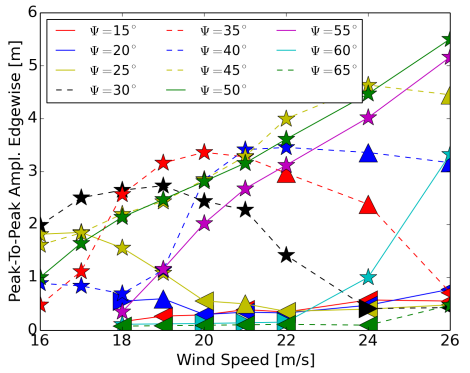

(c) $\mathrm{AOA_{tip}} = 105\,°$, $\mathrm{AOA_{root}} = 87\,°$ (Fixed Pitch), Uniform Inflow, Various Inclination Angles Ψ

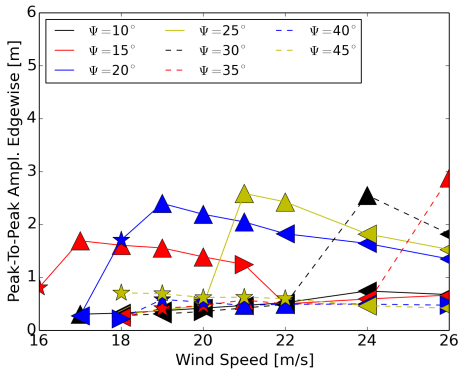

(d) $\mathrm{AOA_{tip}} = 100\,°$, $\mathrm{AOA_{root}} = 82\,°$ (Fixed Pitch), Uniform Inflow, Various Inclination Angles Ψ

Figure 4.46: Max. Edgewise Peak-to-Peak Amplitudes at Blade Tip due to Vortex Induced Vibrations after 45 s of Simulation (1/2),
Left, Up or Right Arrows indicate whether maximum occurs at 1st, 2nd or 3rd part of simulation / Stars indicate continuous amplification

contains the results of simulations for various inclination angles Ψ and different uniform wind speeds. The investigated range of wind speeds starts approximately with the minimum wind speed needed to trigger perceivable vibrations and ends with a wind speed of $V = 26\,m/s$. This limit was chosen in order to confine the number of simulation runs to a feasable amount. Furthermore, a wind speed of $V = 26\,m/s$ is considered to be a reasonable upper limit for eventual wind turbine maintainance tasks and blade mounting activities in which the wind turbine rotor is kept at a fixed position and the yawing system is deactivated. The investigated range of inclination angles is limited to angles between $0\,° \leq \Psi \leq 90\,°$ since this is the region in which the above discussed vortex correlation is expected to trigger vortex shedding of critical frequencies for relatively low to moderate wind speeds. A detailed analysis of other inclination angles and wind speeds was not part of the present investigations.
The presented results comprise computations of pitch and inclination angles in which partially severe edgewise vibrations occur. The outer bounds of this region in terms of pitch is given by Figure 4.46b and Figure 4.47d both showing simulations of pitch angles with no vibrations at all. Assuming that the outer part of the blade is most decisive for the onset of blade vibrations it can be stated that the respective angles of attack of those simulations are relatively far away from the typical 90 degrees setup which, in former studies, was found to be the favourable flow angle for vortex-induced vibrations [36]. It is then interesting to see that in Figure 4.46c for simulations with an angle of attack at the blade tip of $\mathrm{AOA_{tip}} = 105\,°$ the observed blade vibrations increase rapidly and exhibit the highest blade vibrations of the entire test series with inclined inflow. The simulations on the other end of the investigated range of pitch angles with angles

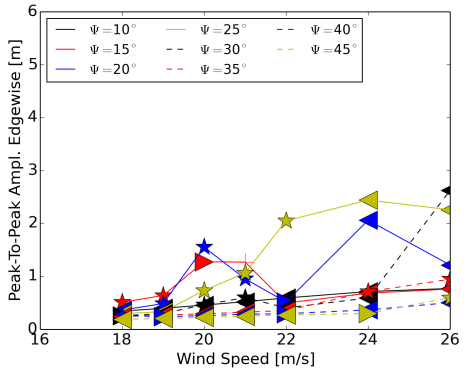

(a) $\mathrm{AOA}_{\mathrm{tip}} = 95\,°$, $\mathrm{AOA}_{\mathrm{root}} = 77\,°$ (Fixed Pitch), Uniform Inflow, Various Inclination Angles Ψ

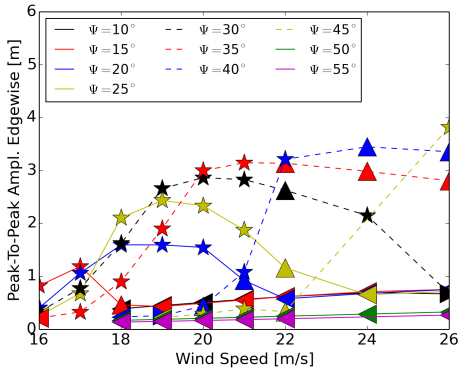

(b) $\mathrm{AOA}_{\mathrm{tip}} = 90\,°$, $\mathrm{AOA}_{\mathrm{root}} = 72\,°$ (Fixed Pitch), Uniform Inflow, Various Inclination Angles Ψ

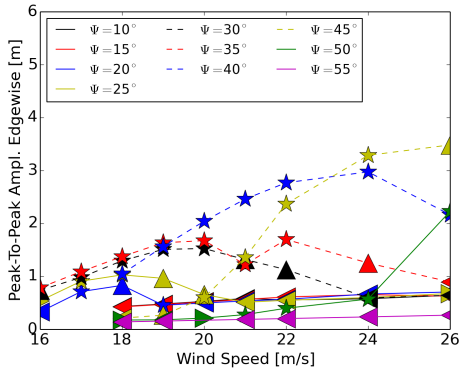

(c) $\mathrm{AOA}_{\mathrm{tip}} = 85\,°$, $\mathrm{AOA}_{\mathrm{root}} = 67\,°$ (Fixed Pitch), Uniform Inflow, Various Inclination Angles Ψ

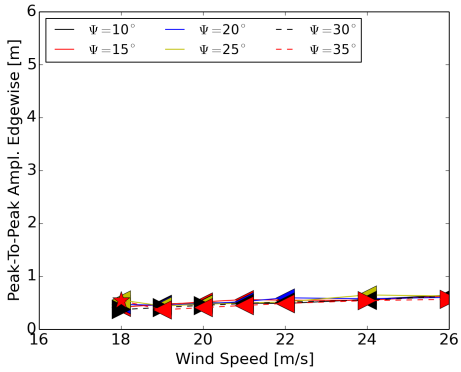

(d) $\mathrm{AOA}_{\mathrm{tip}} = 80\,°$, $\mathrm{AOA}_{\mathrm{root}} = 62\,°$ (Fixed Pitch), Uniform Inflow, Various Inclination Angles Ψ

Figure 4.47: Max. Edgewise Peak-to-Peak Amplitudes at Blade Tip due to Vortex Induced Vibrations after 45 s of Simulation (2/2),
Left, Up or Right Arrows indicate whether maximum occurs at 1st, 2nd or 3rd part of simulation / Stars indicate continuous amplification

of attack at the blade tip of $\mathrm{AOA}_{\mathrm{tip}} = 90\,°$ and $\mathrm{AOA}_{\mathrm{tip}} = 85\,°$ are shown in Figure 4.47b and Figure 4.47c respectively and exhibit relatively strong vibrations as well. The simulations shown in Figure 4.46d and Figure 4.47a with the intermediate angles of attack of $\mathrm{AOA}_{\mathrm{tip}} = 100\,°$ and $\mathrm{AOA}_{\mathrm{tip}} = 95\,°$ also exhibit strong vibrations, however, the response seems to be less pronounced, although large parts of the outer blade exhibit angles of attack close to 90 degrees.
In terms of the inclination angle Ψ it can be seen that an inclination angle of $\Psi \geq 20\,°$ is needed to sufficiently correlate the shed vorticity behind the blade in order to initiate vibrations. For the intermediate angles of attack shown in Figure 4.46d and Figure 4.47a those vibrations persist until an inclination angle of approximately $\Psi = 35\,°$. For the slightly smaller angles of attack in Figure 4.47b and Figure 4.47c vibrations persist until an inclination angle of approximately $\Psi = 45\,°$. For the higher angles of attack in Figure 4.46c severe vibrations persist until an inclination angle of $\Psi = 55\,°$. For certain pitch and inclination angles the smallest investigated wind speed of $V = 16\,m/s$ is enough to trigger vibrations. Generally it can be stated that higher inclination angles require higher wind speeds in order to create resonance. This could be explained with the fact that the projected wind speed perpendicular to the blade decreases with an increased Ψ. It is expected that higher inclination angles can lead to vibrations as well, however, they would require higher wind speeds which lie outside the investigated wind speed range of $16m/s \leq V \leq 26m/s$.

The presented simulations predict severe vortex-induced vibrations for the DTU 10MW RWT blade under realistic inflow conditions during low to moderate wind speeds. The critical range of angles of attack be-

tween $85\,^\circ \leq \mathrm{AOA_{tip}} \leq 105\,^\circ$ can be met during a standstill situation with a blade pitch angle of $\Theta = 90\,^\circ$ in which the wind turbine is exposed to side winds due to a broken or deactivated yawing system. The critical range of inclination angles between $\Psi = 20\,^\circ$ and $\Psi = 55\,^\circ$ can be met when the azimuthal position of the blade enters regions between $125\,^\circ \leq \Phi \leq 160\,^\circ$ or $305\,^\circ \leq \Phi \leq 340\,^\circ$ [3]. Apart from the investigated range of wind speeds, angles of attacks and inclination angles there is the possibility that other critical wind conditions exist as well. Some few investigations with angles of attack close to $\mathrm{AOA_{tip}} = -90\,^\circ$ and $\mathrm{AOA_{tip}} = -130\,^\circ$ i.e. an angle where strong vortex shedding and highly unsteady forces are observed were carried out but did not show any blade vibrations. A detailed investigation of other wind conditions outside the above mentioned boundaries was not part of the present study. Some of the computations with severe and continuously amplified vibrations were rerun for a longer simulation time. After a sufficient simulation time all computations reached a certain limit in edgewise deflection amplitude. However, it is out of the scope of the present work to evaluate the structural impact of those vibrations on the composite materials of a real wind turbine blade.

[3] For an azimuthal position of $\Phi = 0\,^\circ$ the blade is pointing straight upwards

4.4.6 Development of an Engineering Model for Standstill Vibration

The research carried out in the present work package showed that vibrations of wind turbine blades at standstill conditions are a complex subject, and thus require cautious engineering modelling. In principle, the modelling should govern both VIVs and SIVs. In practice however, modelling of VIVs appears to be of higher priority as present work indicated that those vibrations are more likely to occur on wind turbine blades. Among other phenomena, proper modelling of VIVs should govern:

- stochastic modelling of vortex-induced loading on the blade at high angles of attack
- the dependency of the loading and vibration characteristics on the angle of attack and angle of inclination
- the so-called mechanism of lock-in where the frequency of vortex shedding follows the frequency of vibration
- the dependency of the spatial correlation of the loading on the vibration characteristics such as the amplitude and period

The subject of modelling is too complex and broad in order to be finalized within the present project. However, the work is in progress, currently focusing on stochastic modelling of vortex shedding. The current goal is to be able to successfully perform the following procedure:

- Perform a measurement or a 3D CFD computation on an airfoil or a blade to be modelled.
- Read the loading at a high angle of attack.
- Extract characteristic parameters from the time series.
- Using the aforementioned parameters, produce a new and unique time series, statistical characteristics of which resemble those of the original time series. The primary statistical parameters to be resembled are the Probability Distribution Function (PDF) and Frequency Spectrum of the loading.

Because the application of such stochastic modelling is broader than the standstill vibrations, the work is continued on the expense of another EUDP project, namely Blade Dragon. The content of the project includes modelling of the aerodynamic loading on a wind turbine blade suspended on tethers during installation. The scope of the project is to increase the maximum wind speed at which installation may be carried out.

4.5 WP4: Identification of the Importance of Elastic Couplings

Author(s): Taeseong Kim, Vladimir Fedorov

4.5.1 Introduction

Load reduction is one of the key areas necessary to move one step forward for developing very large sized wind turbines (more than 10MW). In order to reduce loads on a turbine many different types of research topics are involved. They can be categorized in two categories: active and passive control methods. For example, the trailing edge flap is the well known active control concept. It has been shown by a full scaled measurement test where the blade root bending load was reduced around 14% [12]. However, this technology requires additional components such as actuators, sensors, etc. On the other hand, changes of the blade geometry and tailoring of the material properties with blade layups can also reduce the loads on a turbine, which falls into the passive control category. The idea of the passive control techniques is to create a coupling between flapwise bending and torsion to decrease or increase the aerodynamic angle of attack locally along the blade. It does not require additional components to reduce loads. It has been shown that the blade flapwise damage equivalent loads can be decreased up to 24% in the 11-13 m/s wind speed range with a material coupling [3]. A geometric coupling, swept blade called STAR (Sweep Twist Adaptive Rotor blade), has been experimentally investigated by Sandia Lab. [4], [2]. From the study it has been shown that the STAR rotor increased average energy capture by 10-12% as compared to the baseline turbines.

In order to understand the physical phenomenon of the passive control methods one should be able to extract the correct structural properties from the structures such as mass and stiffness properties of the blades. However it is not an easy task to compute the structural properties of a wind turbine blade because the blades have complex geometries and are made of combinations of different composite materials with different degrees of anisotropy. Moreover, modern multi-megawatt turbine rotor blades are getting more slender and curved which result in additional structural couplings. Figure 4.48 Timoshenko [44] shows the effects of pre-bending for a case of a curved beam. It is clearly seen that the stress levels are quite different between a straight and a curved beam. Especially, transverse stress is newly introduced in the curved beam resulting from additional couplings between the axial and transverse directions. These structural coupling effects must be taken into account in order to design and analyze a composite blade accurately. In order to generate structural properties, finite element based cross-section analysis tools have been developed by other researchers. [11], [48], [10]. Borri [11] and Yu [48] demonstrated similar effects but not in terms of coupling coefficients in the cross-section stiffness matrix.

In this study, two main topics are investigated: 1) the material coupling effects to estimate load reduction potential without power reduction and 2) the influence of blade twist and curvature effects. In order to consider the material coupling effects, the NREL 5 MW Reference Wind Turbine (RWT) model is used and the DTU 10MW RWT is used for investigating the blade twist and curvature effects. An advanced cross-section analysis tool BECAS [10] is presently modified in order to consider the effects of twist and curvature in beams. The results of the cross-sectional analysis are input into the aeroelastic calculations to obtain and assess dynamic response of the blades in time domain.

4.5.2 Method

Detailed Blade Design of the 5 MW RWT

The existing NREL 5MW RWT does not provide a detailed blade layup configuration which is very important information for creating a material coupling by changing the material layup angles. In order to produce material couplings a detailed structural design has been performed. Three different glass-fiber material configurations are used: Unidirectional, biaxial and triaxial. Seven design points are considered along the cross-sections (see Figure 4.49). In total 53 design points along the blade span are selected for design of the composite layups with which the structural properties such as mass, flapwise stiffness, edgewise stiffness and torsional stiffness, are matched with the published data on blade structural properties.

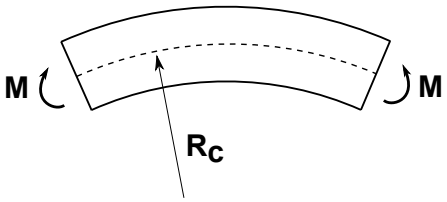

(a) Curved beam in bending

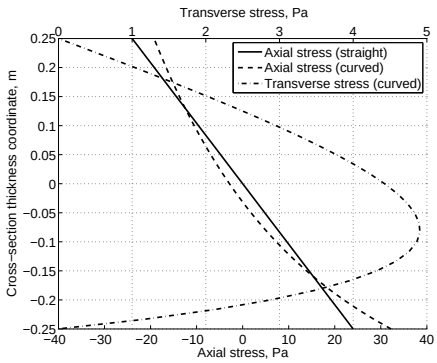

(b) Stresses in straight and curved beams

Figure 4.48: Bending of curved beam with 0.5x1m rectangular cross-section (a) and stress distributions along the cross-section centerline, (b) $R_c = 2/3\,m$ is the beam centerline curvature radius, $M = 1\,Nm$ - bending moment.

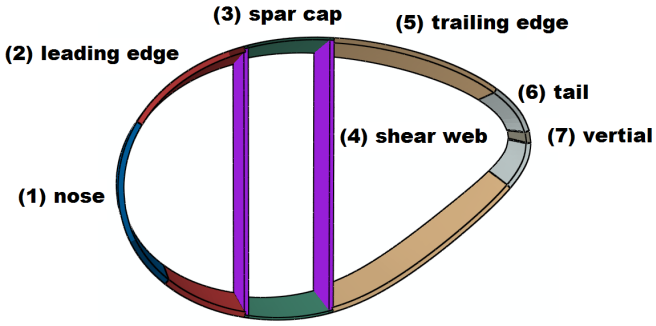

Figure 4.49: Design points on a cross-section

Cross-Sectional Analysis of Curved Beams

The blade structural model is developed using a beam cross-sectional analysis tool BECAS [10]. Originally the tool is capable of calculating all main cross-section parameters, including stiffness matrix for prismatic beams of arbitrary cross-sections with material anisotropy effects taken into account. Presently BECAS has been modified according to Borri [11] in order to account for beam curvature and pre-twist. Validation of the modification has been successfully performed against analytical solutions by Timoshenko and Goodier [44] and numerical solutions from another cross-section analysis tool, VABS, by Yu [48].

Beam geometry

In the present BECAS formulation beam shapes are described as piecewise helicoid, with the curvature vector $\mathbf{c} = const$ fully describing the beam shape. This formulation allows for three types of non-straight beams to be accounted for: Twisted beams ($\mathbf{c} = [0, 0, c_z]^\intercal$), curved beams ($\mathbf{c} = [c_x, 0, 0]^\intercal$ or $\mathbf{c} = [0, c_y, 0]^\intercal$) and twisted and curved beams ($\mathbf{c} = [c_x, 0, c_z]^\intercal$ or $\mathbf{c} = [0, c_y, c_z]^\intercal$), see Fig. 4.50.

Displacements and Strains

Total displacement of a point in beam cross-section is a sum of displacements due to cross-section rigid translations and rotations, $\mathbf{x_{rb}}$ and cross-section deformation (warping), $\mathbf{w}$:

$$\mathbf{x} = \mathbf{x_{rb}} + \mathbf{w} \tag{4.8}$$

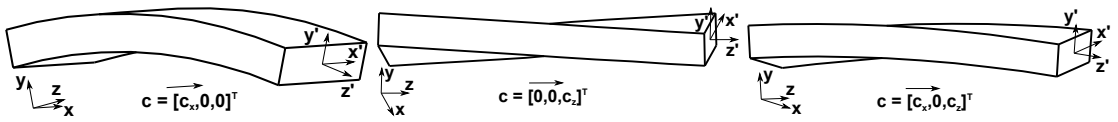

(a) Curved beam (b) Twisted beam (c) Curved and twisted beam

Figure 4.50: Geometry and coordinate systems for curved beams. **xyz** - global (root cross-section) coordinate system, $\mathbf{x'y'z'}$ - current cross-section coordinate system, $\mathbf{c} = const$ - curvature vector.

The cross-section warping displacement field is discretized using appropriate shape functions $\mathbf{N}$ and nodal warping displacements $\mathbf{W}$:

$$\mathbf{w} = \mathbf{NW} \tag{4.9}$$

Further, vectors of generalized cross-section forces $\mathcal{S}$ and deformations $\mathcal{E}$ are written as follows:

$$\mathcal{S} = [F_x,\, F_y,\, F_z,\, M_x,\, M_y,\, M_z]^\intercal \tag{4.10}$$

$$\mathcal{E} = [\epsilon_{xx},\, \epsilon_{yy},\, 2\epsilon_{xy},\, 2\epsilon_{xz},\, 2\epsilon_{yz},\, \epsilon_{zz}]^\intercal \tag{4.11}$$

The virtual work principle

The discretized form of the virtual work principle that relates deformation vectors $\mathcal{E}$, $\mathbf{W}$ (symbol $'$ denotes beam length-wise derivative $\partial/\partial z$) and $\mathbf{W'}$ with the vector of generalized cross-section load $\mathcal{S}$ and nodal loads $\mathbf{P}$ and $\mathbf{P'}$ using matrices $\mathbf{M}$, $\mathbf{C}$ and $\mathbf{E}$ assembled according to typical finite element procedures and matrix of nodal coordinates $\mathbf{Z}$ is written as follows:

$$\begin{bmatrix} \mathbf{M} & \mathbf{C}^\intercal & \mathbf{MZ} \\ \mathbf{C} & \mathbf{E} & \mathbf{CZ} \\ \mathbf{Z}^\intercal\mathbf{M} & \mathbf{Z}^\intercal\mathbf{C}^\intercal & \mathbf{Z}^\intercal\mathbf{MZ} \end{bmatrix} \begin{bmatrix} \mathbf{W'} \\ \mathbf{W} \\ \mathcal{E} \end{bmatrix} = \begin{bmatrix} \mathbf{P} \\ \mathbf{P'} \\ \mathcal{S} \end{bmatrix} \tag{4.12}$$

The matrices $\mathbf{M}$, $\mathbf{C}$ and $\mathbf{E}$ in the system above correspond to the elastic energy of warping deformations stored in the deformed beam. A certain format of the load vector $\mathcal{S}$ allows for the cross-section warping to be sought in form of a linear combination of circular functions on $\phi = c \cdot s$, where c is the curvature vector norm and s is the arc length along the beam axis:

$$\mathbf{W} = \mathbf{U}_0 + \phi\mathbf{V}_0 + (\mathbf{U}_c + \phi\mathbf{V}_c)\cos\phi + (\mathbf{U}_s + \phi\mathbf{V}_s)\sin\phi, \tag{4.13}$$

Cross-section strains $\mathcal{E}$ are also sought in the same form.

Boundary conditions

By applying proper boundary conditions to exclude the redundancy coming from (4.8) and solving the system (4.12) for six independent unit load cases the corresponding solutions for warping $\mathbb{W}$, the warping derivative $\mathbb{W}'$ and strain $\mathbb{E}$ are obtained.

Cross-section stiffness matrix

Based on the solutions obtained above the cross-section stiffness matrix is calculated as follows:

$$\mathbf{K} = \left(\begin{bmatrix} \mathbb{W}' \\ \mathbb{W} \\ \mathbb{E} \end{bmatrix}^\intercal \begin{bmatrix} \mathbf{M} & \mathbf{C}^\intercal & \mathbf{MZ} \\ \mathbf{C} & \mathbf{E} & \mathbf{CZ} \\ \mathbf{Z}^\intercal\mathbf{M} & \mathbf{Z}^\intercal\mathbf{C}^\intercal & \mathbf{Z}^\intercal\mathbf{MZ} \end{bmatrix} \begin{bmatrix} \mathbb{W}' \\ \mathbb{W} \\ \mathbb{E} \end{bmatrix} \right)^{-1} \tag{4.14}$$

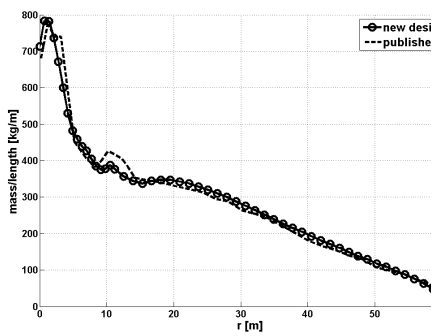

(a) Mass per lenght distribution

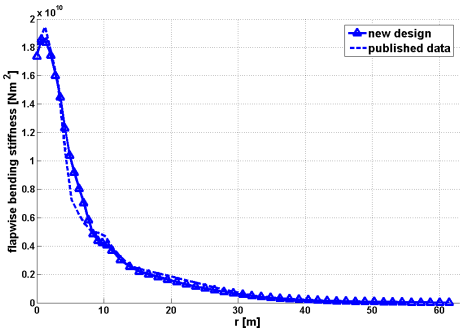

(b) Flapwise stiffness distribution

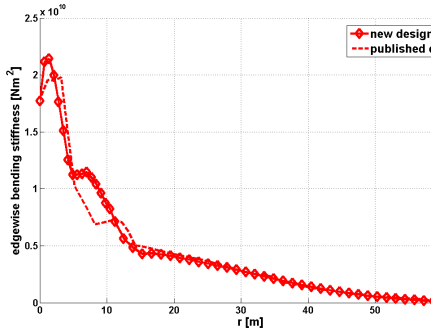

(c) Edgewise stiffness distribution

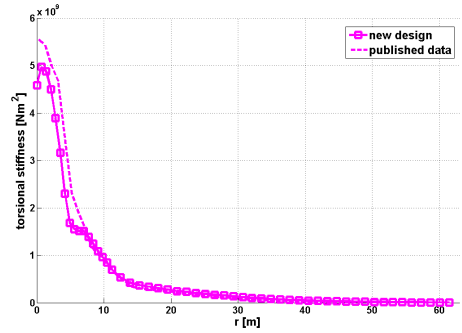

(d) Torsional stiffness distribution

Figure 4.51: Comparison of structurla peoperties between the published data and the obtained data

Aeroelastic Calculations

Aeroelastic calculations for the material coupling effects and the blade curvature effects are presently performed using aeroelastic code HAWC2[22]. HAWC2 is an aeroelastic nonlinear multi-body code for calculating wind turbine response in time domain. A fully coupled beam finite element that accounts for effects of material anisotropy has been developed earlier by Kim[21]. This finite element is used in the study for modeling blades in the aeroelastic calculations. Hereby, the blade 6x6 cross-section stiffness matrices calculated using BECAS serve as an input to produce 12x12 beam finite element stiffness matrices. For investigation on the effects of blade pre-bending the results of both BECAS versions, with and without accounting for beam curvature and twist, are used and, thus, two parallel computations are presently performed.

4.5.3 Results for the Material Coupling Effects

Structural Design of 5MW RWT Blade

A total of 53 design points are considered to design the composite layups with which the given structural properties are duplicated. In this study four structural properties were considered to be matched; mass per length, flapwise bending stiffness, edgewise bending stiffness, and torsional stiffness. Figure4.51 shows the computed structural property distributions compared with the published data. As shown, the obtained structural properties are matched very well. In order to estimate the differences between two models eigenvalue analysis has been performed with the blade only as well as the whole turbine. Table 4.4 shows the comparisons between the baseline (original 5MW RWT) and the new design. The lower modes show good agreement.

Table 4.4: Eigenvalue analysis

	Whole turbine natural frequency		Blade natural frequency	
Mode number	Baseline [Hz]	New design [Hz]	Baseline [Hz]	New design [Hz]
1	0.32	0.32	0.65	0.66
2	0.32	0.32	1.00	1.07
3	0.62	0.62	1.81	1.99
4	0.64	0.65	3.19	3.83
5	0.68	0.70	3.88	4.43
6	1.00	1.06	5.80	7.54

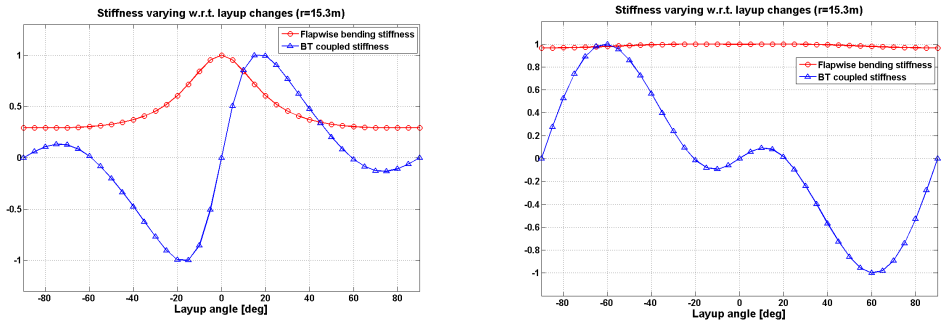

(a) Stiffness varying with respect to skin and spar cap layup angle changes

(b) Stiffness varying with respect to skin layup angle changes

Figure 4.52: Stiffness changes due to blade layup changes

Sensitivity Analysis

In order to find the maximum coupling amount a sensitivity analysis has been conducted. Layup angles for leading and trailing edges of the blade, called skin, and spar caps (see Figure4.49) are varied from -90 to 90 deg. Figure4.52 shows the stiffness variation with respect to layup changes on a section placed $15.3m$ from the blade root. It is clearly seen that when the bending-twist coupling effect is increased the main flapwise bending stiffness is decreased. When the layup angles on blade skin and spar caps varied the maximum coupling is obtained with $\pm 15deg$ layup. The maximum bending-twist coupling is obtained at $\pm 60deg$ when the skin layup is only varied.

Based on the sensitivity analysis a parametric study has been performed. Table 4.5 shows the considered 9 cases. Only a single wind speed, $10m/s$, with 18% turbulence intensity is considered. Tower shadow and wind shear are also considered. Blade root flapwise equivalent fatigue load ($m = 12$), blade tip deflection, and electrical power are compared (see Figure 4.53).

From the results, it is very clear to see that the considered bending-twist couplings are able to reduce the blade fatigue loads from 4 to 15%. At the same time the maximum blade tip deflections are increased due to a decrease in the flapwise bending stiffness. On the other hand, the electrical power does not change much. From the results, Case 6 has been selected to simulate the full wind speed range with the normal turbulence model from 4 to $24m/s$ with $2m/s$ increments. The reason for selecting Case 6 is that the flapwise fatigue load is reduced around 10% without increasing the maximum blade tip deflection considerably. Figure 4.54 shows the equivalent blade flapwise loads, electrical power, and the maximum blade tip deflection comparisons between the original 5MW RWT and Case 6 during normal operation conditions. The blade flapwise equivalent fatigue loads are reduced without power loss, and the maximum blade tip deflection is increased less than $1m$.

From this study it can be concluded that there is a large potential to reduce the blade loads without losing power and increasing blade tip deflection.

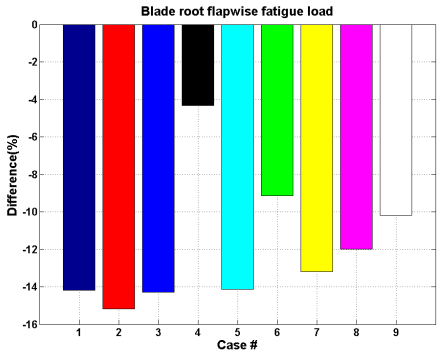

(a) Blade root flapwise equivalent fatige loads

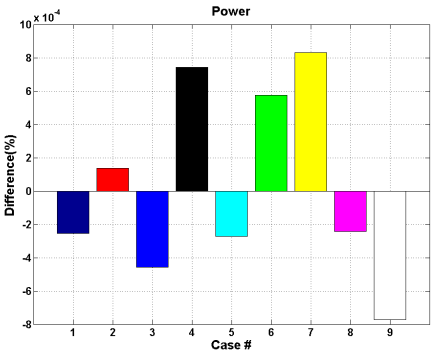

(b) Electrical powers

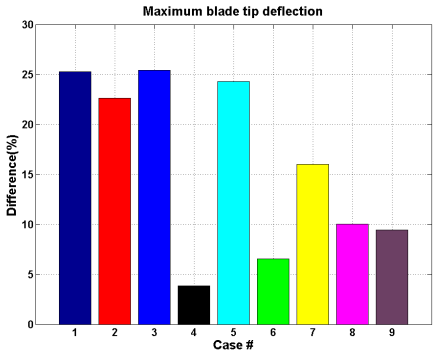

(c) Maximum blade tip deflections

Figure 4.53: Parametric study results

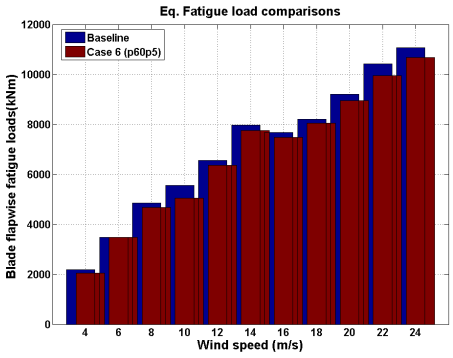

(a) Blade root flapwise equivalent fatige loads

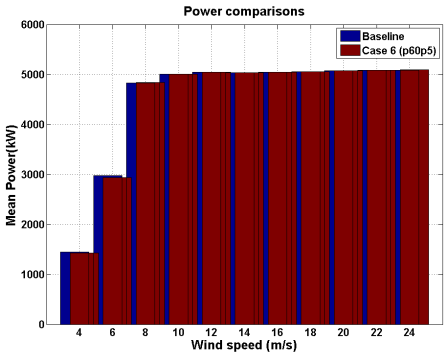

(b) Electrical powers

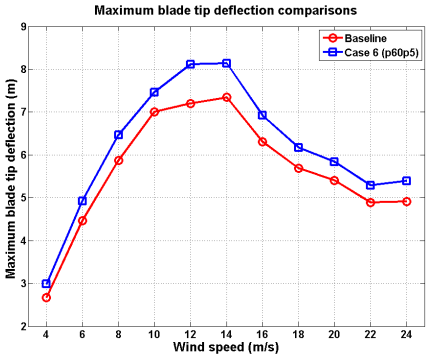

(c) Maximum blade tip deflections

Figure 4.54: Comparison results in normal operation condition

Table 4.5: List of considered cases

	Skin [deg]	Spar caps [deg]
Case1	15	15
Case2	15	-15
Case3	-15	15
Case4	60	0
Case5	0	15
Case6	60	5
Case7	60	10
Case8	10	10
Case9	-10	-10

Table 4.6: BECAS result validation

	Borri	VABS	BECAS	BECAS vs Borri
Main diagonal components				
K_{11}	2.070e6	2.070e6	2.071e6	0.0%
K_{22}	2.070e6	2.070e6	2.071e6	0.0%
K_{33}	6.500e6	6.500e6	6.500e6	0.0%
K_{44}	1.350e5	1.350e5	1.354e5	0.3%
K_{55}	1.350e5	1.350e5	1.354e5	0.3%
K_{66}	8.790e4	8.790e4	8.787e4	0.0%
Off-diagonal components				
Curved beam, $\mathbf{c} = [0.05, 0, 0]^\intercal$				
K_{16}	2.180e3	-2.260e3	2.178e3	-0.1%
K_{34}	-9.340e3	-8.800e3	-9.340e3	0.0%
Twisted beam, $\mathbf{c} = [0, 0, 0.05]^\intercal$				
K_{14}	-1.360e3	-1.360e3	-1.356e3	0.3%
K_{25}	-1.360e3	-1.360e3	-1.356e3	0.3%
K_{36}	2.120e3	2.120e3	2.118e3	-0.1%
Curved and twisted beam, $\mathbf{c} = [0, 0.05, 0.05]^\intercal$				
K_{14}	-1.360e3	-1.360e3	-1.356e3	0.3%
K_{25}	-1.360e3	-1.360e3	-1.357e3	0.2%
K_{26}	2.180e3	2.260e3	2.178e3	-0.1%
K_{32}	2.530e2	2.530e2	2.526e2	-0.2%
K_{35}	-9.340e3	-8.800e3	-9.338e3	0.0%
K_{36}	2.120e3	2.120e3	2.118e3	-0.1%

4.5.4 Results for the Effects of Curvature

Cross-Sectional Analysis

The developed version of the BECAS code is validated against the original formulation by Borri et.al.[11] and another finite element code VABS by Yu et.al.[48]. Three cases for a beam made of isotropic material are considered for (from Yu et.al. [48]): A curved beam with $\mathbf{c} = [0.05, 0, 0]^\intercal$, a twisted beam with $\mathbf{c} = [0, 0, 0.05]^\intercal$ and a curved and twisted beam with $\mathbf{c} = [0, 0.05, 0.05]^\intercal$. Table 4.6 shows the comparison results between the developed code and the references in terms of components of the beam cross-section stiffness matrix. It shows perfect agreement with the code by Borri et. al. [11] and VABS by Yu [48] with an error of only up to 0.3%.

Eigenvalue Analysis

Eigenvalue analysis for the DTU 10MW blade has been conducted by considering the effect of curvature. Table 4.7 shows the eigenvalue comparisons between considering curvature effect, called curved, and ig-

Table 4.7: Eigenvalue analysis

	Straight [Hz]	Curved [Hz]
1st Flap	0.61	0.61
1st Edge	0.93	0.93
2st Flap	1.74	1.74
2st Edge	2.76	2.76
3st Flap	3.57	3.58
3st Edge	5.67	5.66
4th Flap	6.12	6.14
4th Edge	6.66	6.66

noring it, called straight. Overall, frequencies do not change significantly. Only higher modes are slightly changed. It is because the additional coupling effects are too small resulting from the blade curvature.

Dynamic Responses Due to the Curvature of the DTU 10MW RWT Blade

Cross-section stiffness matrices for DTU 10MW RWT blade without accounting for the twist and curvature effects, $\mathbf{K_{straight}}$, and with the effects taken into account, $\mathbf{K_{curved}}$, are directly compared. Figure 4.55 shows one of the blade cross-sections, namely the one located at $L = 24.61$ meter away from the blade root. Stiffness matrices, $\mathbf{K_{straight}}$ and $\mathbf{K_{curved}}$, for this cross-sections are presented further in 4.15 and 4.16 respectively:

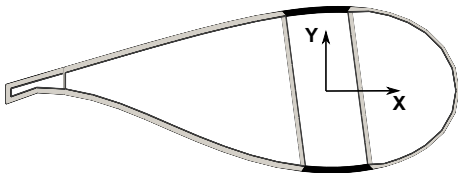

Figure 4.55: Blade cross-section 24.6 m away from the blade root. Dark-gray colors correspond to fiberglass materials, light-gray – sandwich core. Large dark areas – uni-directional fibers at the the spar caps.

$$\mathbf{K_{straight}} = \begin{bmatrix} 7.177E8 & -5.621E7 & \mathbf{0} & \mathbf{0} & \mathbf{0} & -1.529E8 \\ -5.621E7 & 5.366E8 & \mathbf{0} & \mathbf{0} & \mathbf{0} & 6.975E8 \\ \mathbf{0} & \mathbf{0} & 9.185E9 & 3.172E8 & -6.971E9 & \mathbf{0} \\ \mathbf{0} & \mathbf{0} & 3.172E8 & 8.269E9 & 8.810E8 & \mathbf{0} \\ \mathbf{0} & \mathbf{0} & -6.971E9 & 8.810E8 & 2.394E10 & \mathbf{0} \\ -1.529E8 & 6.975E8 & \mathbf{0} & \mathbf{0} & \mathbf{0} & 2.659E9 \end{bmatrix} \tag{4.15}$$

$$\mathbf{K_{curved}} = \begin{bmatrix} 7.191E8 & -5.603E7 & \mathbf{8.932E5} & \mathbf{-2.570E7} & \mathbf{-1.697E6} & -1.514E8 \\ -5.603E7 & 5.375E8 & \mathbf{2.091E7} & \mathbf{-4.163E6} & \mathbf{-8.669E7} & 6.983E8 \\ \mathbf{8.932E5} & \mathbf{2.091E7} & 9.189E9 & 3.052E8 & -6.997E9 & \mathbf{9.952E7} \\ \mathbf{-2.570E7} & \mathbf{-4.163E6} & 3.052E8 & 8.337E9 & 8.891E8 & \mathbf{-6.061E6} \\ \mathbf{-1.697E6} & \mathbf{-8.669E7} & -6.997E9 & 8.891E8 & 2.400E10 & \mathbf{-1.733E7} \\ -1.514E8 & 6.983E8 & \mathbf{9.952E7} & \mathbf{-6.061E6} & \mathbf{-1.733E7} & 2.662E9 \end{bmatrix} \tag{4.16}$$

It is clearly seen that the stiffness matrix for the case where blade twist and curvature are accounted for is fully populated in contrast to $\mathbf{K_{straight}}$. This shows additional couplings that are present in the system due to the blade twist and curvature.

In order to compare the coupling effects provided by the blade twist and curvature a normal turbulence case with single turbulence seed from 5 to 25m/s with 2 m/s increase is numerically simulated using HAWC2. Blade root bending moments (see Figure 4.56) and tower bottom bending moments (see Figure 4.57) are

compared. As seen from the figures, only very small differences are observed. Figure 4.58 shows the small difference more clearly. The differences are not significant. However the coupling effects might be increased when the blade is swept or tailored with different layup angles.

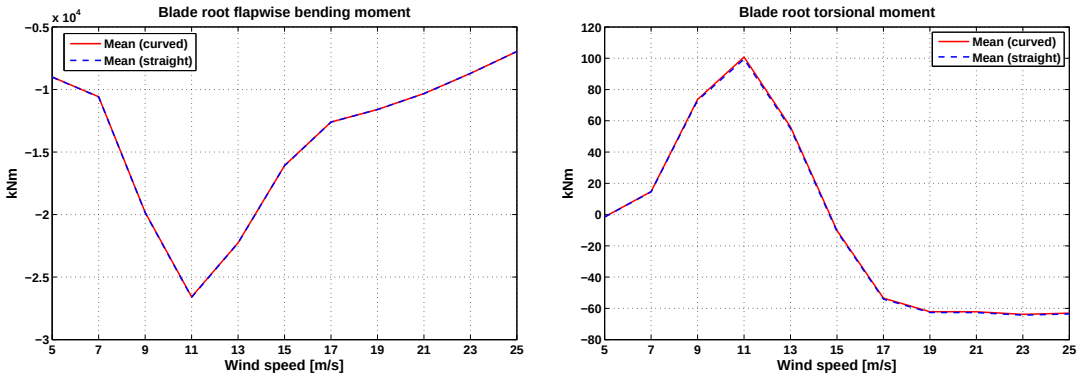

(a) Blade root flapwise bending moment

(b) Blade root torsional moment

Figure 4.56: Blade root bending moments (a) Blade root flapwise bending moment, (b) Blade root torsional moment.

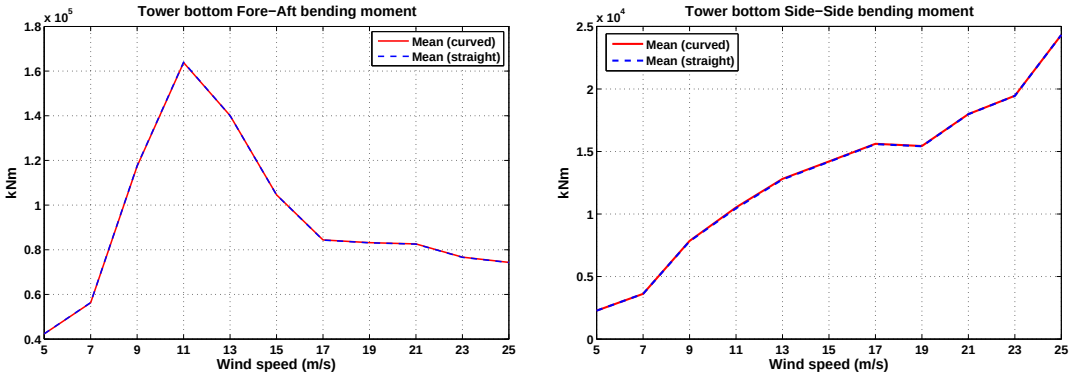

(a) Tower bottom fore-aft bending moment

(b) Tower bottom side-side bending moment

Figure 4.57: Tower bottom bending moments (a) Fore-aft bending moment, (b) Side-side bending moment.

4.5.5 Conclusions

In this section, a load reduction potential with material couplings has been studied. In order to introduce the material couplings a detailed blade structural design of the NREL 5MW RWT has been conducted with glass fiber material. Through the sensitivity and parametric studies by changing the layup angles one case is selected with a 60 deg layup angle for the leading and trailing edge and a 5 deg layup angle for the spar caps are applied. In order to investigate the load reduction potential normal operation conditions from $4m/s$ to $24m/s$ with $2m/s$ increments with the normal turbulence model are considered. The blade flapwise equivalent loads, the maximum blade tip deflections, and electrical power are compared with the original 5MW RWT. The blade flapwise equivalent fatigue loads are reduced up to 9% without reducing the electrical power with the considered material coupling case. The maximum blade tip deflection is only increased around $1m$. From this investigation it can be concluded that there is a large potential to reduce blade equivalent fatigue loads without loosing electrical power and increasing maximum blade tip deflections.

The beam curvature and pre-twist effects have been investigated and implemented into BECAS. Three

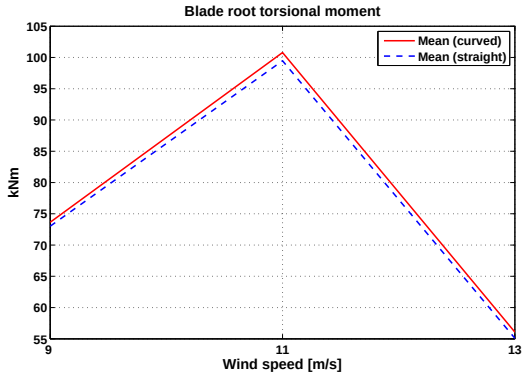

(a) Blade root torsional moment - zoom

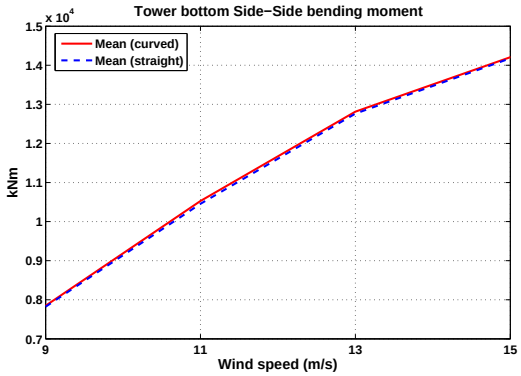

(b) Tower bottom side-side bending moment - zoom

Figure 4.58: Blade amd tower bending moments - zoomed (a) Blade root torsional moment - zoomed, (b) Tower bottom side-side bending moment - zoomed.

different cases, curved, twisted, and curved and twisted, are considered for comparing the updated BECAS with the existing models. It was seen that all cases were agreed very well. Also it was clearly seen that the additional structural coupling effects are introduced due to the curvature and pre-twist of the beam. However the dynamic responses due to the additional coupling terms resulting from the blade curvature do not change significantly because the amount of couplings are relatively small. However the coupling effects might be increased when the blade is swept or tailored with different layup angles. Also the additional coupling terms due to the blade geometries, curved and pre-twisted, should be considered in order for designing and analyzing the dynamic response of the large blade accurately.

5 Utilization of project results

The scientific articles that have been produced as a result of the project are expected to help retain DTU Wind Energy as a leading institution for research in Wind Energy. In addition to this, publications are central for DTU Wind Energy to be able to secure future funding, both commercial and government based.

A number of the results of the project are expected to be suitable for both continued usage and further development in a research context as well as for commercial utilization: The model developed to simulate vortex generators in EllipSys3D is at this stage already being used in other scientific projects (EUDP "Partial Pitch 2-Bladed wind turbine demonstration project", EU "AVATAR" and others). In addition to this the model will become available to commercial end-users of EllipSys3D (among them LM Wind Power). The coupled solver HAWC2CFD used to investigate standstill vibrations marks an important milestone for both CFD and aeroelastic modelling of wind turbines. The model will be used to continue investigations into complex flow phenomena such as those governing the dynamics of a wind turbine at standstill. The results of the project uncovered that highly complex dynamics are at play, which resulted in the decision to postpone the development of an engineering model for vortex induced vibration until a better understanding of the problem has been gained. In addition to this, due to flexibility of the coupling, the model is currently also in use in the project "Single Blade Installation in high Wind Speeds" to investigate the dynamics of a blade during the mounting process, where in fact it has been shown that the aerodynamics used in the standard HAWC2 code based on BEM is far from adequate to capture the complex flow phenomena at play. The 40% aerofoil designed and tested in the project will enter the portfolio of the commercial partners and could if found suitable be used on future turbine blades. The aerofoil design tool developed in this project marks a new step in aerofoil design since 2D CFD can now with very little knowledge of CFD be used by aerofoil designers. The tool including EllipSys2D as the flow engine is expected to be made commercially available in 2015.

From the commercial partners' perspective, all the knowledge and data, which has been gathered during the course of the project helps LM Wind Power in the daily work. Thick flatback airfoils will be growing in stock in the LM airfoil portfolio as this is considered to be the right choice for future thick airfoil designs. Therefore it is crucial to LM Wind Power that design and testing of thick airfoils can be done with high accuracy, so that optimal designs of each individual airfoil can be achieved in order to boost the Annual Energy Production (AEP) on blades, which will result in increased competitiveness on the blade market, which is absolutely essential to LM Wind Power in order to maintain and increase its market share. The work done in this project has helped LM Wind Power to gain understanding of the problems associated with designing and testing of thick airfoils for wind turbine blades, and even though there is still a lot to be done in order to design optimal thick airfoil shapes, this project has been a step in the right direction.

6 Project Conclusions and Perspectives

The present project has tackled a number of current challenges faced in analysis and design of wind turbines through a collaborative effort between DTU Wind Energy and two industrial partners. The primary outcomes of the project are increased knowledge within the different areas addressed in the project as well as newly developed models used to more accurately simulate the performance of wind turbines numerically as well as improved techniques to experimentally measure aerofoils in wind tunnels. Improved simulation tools are central to the advancement of wind turbine design since a reduction in the uncertainty of the models used in the design process allows on one hand wind turbine designers to reduce the safety margins on various parts of the design as well as explore new design solutions not previously feasible due to inadequate modelling tools.

The focus on the measurement on and performance of thick aerofoils in work package 1 has resulted in improved accuracy of the LM Low Speed Wind Tunnel in particular for thick aerofoils. The flow in the tunnel was measured in detail, which makes it possible to more accurately simulate aerofoils mounted in the tunnel using a 3D CFD solver, where the effects of the side walls can be investigated. A new aerofoil with 40% chord thickness was designed using a newly developed CFD based design tool, designed to meet aggressive structural constraints needed for the inner part of a wind turbine blade. The aerofoil was tested in the LM LSWT using the improved wind tunnel measurement techniques developed during the project.

In work package 2 data from the DANAERO experiment was analysed with focus on the inboard thick aerofoils and compared to both numerical predictions and wind tunnel measurements on the aerofoils. 3D aerofoil data was also computed for the DTU 10MW RWT using various methods, where it was shown that most engineering models are challenged for the very in-board aerofoils, indicating that 3D CFD based methods are most suitable. A cost-effective and easy to use model for including vortex generators in 3D rotor CFD simulations was developed, and validated against high accuracy wind tunnel measurements.

Work package 3 addressed the dynamics of standstill blade vibrations. Different methods of calculating 360 degree airfoil data were developed, where both 3D CFD of a single blade of the DTU 10MW RWT, engineering models and wind tunnel measurements were explored. High-fidelity aeroelastic simulations coupling 3D CFD with an aeroelastic code were used both on a geometrically simple blade section as well as on a fully resolved representation of a blade to investigate stall induced and vortex induced vibration phenomena on wind tubines. The investigations showed that standstill vibrations can occur on modern wind turbines, most likely dominated by vortex induced vibrations. This finding shows that current aeroelastic codes based on Blade Element Momentum theory has an important deficiency in predicting this type of failure.

In work package 4 the potentials for introducing geometric and material couplings in blades for alleviating fatigue loads were investigated. A new structural model taking into account taper and curvature of blades was implemented, and new structural designs of a 10 MW blade were investigated showing a potential for up to 10% reductions in blade root fatigue loads using a structurally tailored design.

Overall, the project has resulted in a number of new numerical models and scientific results that will be further developed and used in future research projects, and for some cases already are in use. Further exploration of thick aerofoil design is necessary, where recent developments in design tools now allow for simultaneous optimization of the blade structural design and the aerodynamic design of a wind turbine blade, thus bridging the gap between the work carried out in WP1 and WP4. While the new model for vortex generators for CFD was not demonstrated for rotors this milestone will be achieved in the near future, and will allow for derivation of 3D CFD based aerofoil data including the effects of vortex generators, which to the best of the authors' knowledge has not been achieved before. The state-of-the art aeroelastic tool HAWC2CFD was used to investigate standstill vibrations, but is already in use in other projects e.g. the EUDP funded "Single Blade Installation in high Wind Speeds". It is anticipated that the tool will become a standard in CFD rotor simulations within a short time scale given the continuous increase in computational resources.

Bibliography

[1] OpenMDAO. URL http://openmdao.org.

[2] T. D. Ashwill. Sweep-twist adaptive rotor blade: Final project report. Technical Report SAND2009-8037, Sandia National Laboratories, 2010.

[3] T. D. Ashwill. Passive Load Control for Large Wind Turbines. *51st AIAA/ASME/ASCE/AHS/ASC Structural Dynamics, and Materials Conference*, 2010.

[4] T. D. Ashwill, G. Kanaby, K. Jackson, and M. Zuteck. Development of the Swept Twist Adaptive Rotor (STAR) Blade. *48th AIAA Aerospace Sciences Meeting*, 2010.

[5] P. Bæk. Experimental Detection of Laminar to Turbulent Boundary Layer Transition on Airfoils in an Industrial Wind Tunnel Facility. Master's thesis, The Technical University of Denmark DTU, September 2008.

[6] C. Bak, J. Johansen, and P. Andersen. Three-Dimensional Corrections of Airfoil Characteristics Based on Pressure Distributions. *European Wind Energy Conference, Athens*, 2006.

[7] C. Bak, F. Zahle, R. Bitsche, T. Kim, A. Yde, L. Henriksen, P. Andersen, A. Natarajan, and M. Hansen. Design and performance of a 10 MW wind turbine. *To be submitted for Wind Energy*, 2014.

[8] A. Bechmann, N. Sørensen, J. Berg, J. Mann, and P.-E. Réthoré. The Bolund Experiment, Part II: Blind Comparison of Microscale Flow Models. *Boundary Layer Meteorology*, 141(2):245–271, 2011.

[9] J. P. Blasques. User's manual for BECAS - a cross section analysis tool for anisotropic and inhomogeneous beam sections of arbitrary geometry. Technical report, DTU Wind Energy, Roskilde, 2013.

[10] J. P. Blasques and M. Stolpe. Multi-material topology optimization of laminated composite beam cross sections. *Composite Structures*, 94:3278–3289, 2012.

[11] M. Borri, G. L. Ghiringhelli, and T. Merlini. Lenear analysis of naturally curved and twisted anisotropic beams. *Composites Engineering*, 2(5-7):433–456, 1992.

[12] D. Castaignet, T. Barlas, T. Buhl, N. K. Poulsen, J. J. Wedel-Heinen, N. A. Olesen, C. Bak, and T. Kim. Full-scale test of trailing edge flaps on a Vestas V27 wind turbine: active load reduction and system identification. *Wind Energy*, 2013.

[13] P. Chaviaropoulos and M. Hansen. Investigating Three-Dimensional and Rotational Effects on Wind Turbine Blades by Means of a Quasi-3D Navier Stokes Solver. *Fluids Engineering*, 122:330–336, 2000.

[14] J. M. Chen and Y.-C. Fang. Strouhal Numbers of Inclined Flat Plates. *Journal of Wind Engineering and Industrial Aerodynamics*, 61(2):99–112, 1996. ISSN 01676105. doi: 10.1016/0167-6105(96)00044-X. URL http://linkinghub.elsevier.com/retrieve/pii/016761059600044X.

[15] Z. Du and M. Selig. A 3-D Stall-Delay Model for Horizontal Axis Wind Turbine Performance Prediction. *AIAA-98-0021, 36th AIAA Aerospace Sciences Meeting and Exhibit, ASME Wind Energy Symposium, Reno, NV, USA, January 12-15*, 1998.

[16] H. Dumitrescu, V. Cardo\cs, and A. Dumitrache. Modelling of inboard stall delay due to rotation. *Journal of Physics: Conference Series*, 75, 2007.

[17] J. Heinz, N. Sørensen, and F. Zahle. Fluid-Structure Interaction Computations for Geometrically Resolved Rotor Simulations Using CFD (in review process). *Wind Energy*, 2014.

[18] J. Heinz, N. Sørensen, F. Zahle, and W. Skrzypiński. Vortex-Induced Vibrations on a Modern Wind Turbine Blade (in review process). *Wind Energy*, 2014.

[19] J. Johansen and N. Sørensen. Airfoil characteristics from 3D CFD rotor computations. *Wind Energy*, 7, 2004.

[20] J. Johansen, N. Sørensen, and R. Mikkelsen. *Rotoraerodynamik*, volume Risø-R-1434(DA), pages 11–34. 2004. ISBN 87-550-3272-9.

[21] T. Kim, A. M. Hansen, and K. Branner. Development of an anisotropic beam finite element for composite wind turbine blades in multibody system. *Renewable Energy*, 59:172–183, 2013.

[22] T. Larsen and A. Hansen. How 2 hawc2, the user's manual. Technical Report Technical Report Risø -R-1597(ver. 4-3)(EN), Risø National Laboratory, 2012.

[23] C. Lindenburg. Modelling of rotational augmentation based on engineering considerations and measurements. *European Wind Energy Conference, London*, 2004.

[24] F. Menter. Zonal Two Equation k-ω Turbulence Models for Aerodynamic Flows. *AIAA Journal*, (93-2906), 1993.

[25] F. Menter, R. Langtry, S. Likki, Y. Suzen, P. Huang, and S. Völker. A Correlation-Based Transition Model Using Local Variables, Part I - Model Formulation. *Proc. of ASME Turbo Expo, Power for Land, Sea and Air. Vienna, Austria*, 2004.

[26] F. Menter, R. Langtry, S. Likki, Y. Suzen, P. Huang, and S. Völker. A Correlation-Based Transition Model Using Local Variables, Part II - Test cases and Industrial Applications. *Proc. of ASME Turbo Expo, Power for Land, Sea and Air. Vienna, Austria*, 2004.

[27] J. Michelsen. Basis3D - a platform for development of multiblock PDE solvers. Technical report AFM 92-05, Technical University of Denmark, Lyngby, 1992.

[28] J. Michelsen. Block structured multigrid solution of 2D and 3D elliptic PDEs. Technical Report AFM 94-06, Technical University of Denmark, 1994.

[29] J. A. Michelsen. Basis3D—a platform for development of multiblock PDE solvers. Technical Report AFM 92-05, Technical University of Denmark, 1992.

[30] J. A. Michelsen. Block structured multigrid solution of 2D and 3D elliptic PDEs. Technical Report AFM 94-06, Technical University of Denmark, 1994.

[31] H. M.O.L. and J. Johansen. Tip studies using CFD and computation with tip loss models. *Wind Energy*, 7, 2004.

[32] H. D. Papenfuß. Aerodynamic Commissioning of the New Wind Tunnel at LM Glasfiber A/S (Lunderskov); Private Communication. Property of LM Glasfiber, June 2006.

[33] P.-E. Réthoré and N. N. Sørensen. A discrete force allocation algorithm for modelling wind turbines in computational fluid dynamics. *Wind Energy*, 15:915–926, 2012.

[34] P.-E. Réthoré, P. van der Laan, N. Troldborg, F. Zahle, and N. N. Sørensen. Verification and validation of an actuator disc model. *Wind Energy*, 2013.

[35] W. Skrzypinski, F. Zahle, and C. Bak. Parametric approximation of airfoil aerodynamic coefficients at high angles of attack. In *European Wind Energy Conference & Exhibition 2014*, 2014.

[36] W. Skrzypiński, M. Gaunaa, N. Sørensen, F. Zahle, and J. Heinz. Vortex-induced vibrations of a du96-w-180 airfoil at 90 deg angle of attack. *Wind Energy*, 17(10):1495–1514, 2014. ISSN 1099-1824. doi: 10.1002/we.1647. URL http://dx.doi.org/10.1002/we.1647.

[37] W. R. Skrzypiński, M. Gaunaa, N. Sørensen, F. Zahle, and J. Heinz. Self-induced vibrations of a du96-w-180 airfoil in stall. *Wind Energy*, 17(4):641–655, 2014. ISSN 1099-1824. doi: 10.1002/we.1596. URL http://dx.doi.org/10.1002/we.1596.

[38] H. Snel, R. Houwink, G. van Bussel, and A. Bruining. Sectional Prediction of 3D Effects for Stalled Flow on Rotating Blades and Comparison with Measurements. *Proc. European Community Wind Energy Conference, Lübeck-Travemünde, Germany, 8-12 March*, pages 395–399, 1993.

[39] N. Sørensen. *General Purpose Flow Solver Applied to Flow over Hills*. PhD thesis, Technical University of Denmark, 1995.

[40] N. Sørensen, F. Zahle, C. Bak, and T. Vronsky. Prediction of the Effect of Vortex Generators on Airfoil Performance. *Torque conference 2014, Lyngby, Denmark*, 2014.

[41] N. N. Sørensen. General purpose flow solver applied to flow over hills. Technical Report Risø-R-827(EN), Risoe National Laboratory, 1995.

[42] N. N. Sørensen, A. Bechmann, and F. Zahle. 3D CFD computations of transitional flows using DES and a correlation based transition model. *Wind Energy*, 14, 2011.

[43] N. N. Sørensen. CFD modelling of laminar-turbulent transition for airfoils and rotors using the γ-re_θ model. *Wind Energy*, 12(8):715–733, 2009. ISSN 10991824, 10954244. doi: 10.1002/we.325.

[44] S. P. Timoshenko and J. N. Goodier. *Theory of Elastisity*. McGraw-Hill, Maiden-head, UK, 1970.

[45] J. Van Ingen and M. Kotsonis. A Two-Parameter Method for eN Transition Prediction.

[46] W. Würz, P. B., C. Vetter, and M. Langohr-Kolb. Wind tunnel measurements of the FFA-W3-301 and FFA-W3-360 airfoils with vortex generators and gurney flaps. Technical report, Institut Für Aerodynamik und Gasdynamik, Universität Stuttgart, IAG, 2013.

[47] S. W.Z., H. M.O.L., and S. rensen J.N. Determination of the angle of attack on rotor blades. *Wind Energy*, 12, 2009.

[48] W. Yu, D. H. Hodges, V. Volovoi, and C. E. S. Cesnik. On timoshenko-like modeling of initially curved and twisted composite beams. *International Journal of Solids and Structures*, 39(19):5101–5121, 2002.

[49] F. Zahle, C. Bak, S. Guntur, N. Sørensen, and N. Troldborg. Comprehensive aerodynamic analysis of a 10 mw wind turbine rotor using 3d cfd. *32nd ASME Wind Energy Symposium*, 2014.

[50] F. Zou, V. Riziotis, S. Voutsinas, and J. Wang. Analysis of Vortex-Induced and Stall-Induced Vibrations at Standstill Conditions Using a Free Wake Aerodynamic Code. *Wind Energy*, pages n/a–n/a, 2014. ISSN 10954244. doi: 10.1002/we.1811. URL http://doi.wiley.com/10.1002/we.1811.